Thin–Walled Structures 203 (2024) 112141

Contents lists available at ScienceDirect

Thin-Walled Structures

journal homepage: www.elsevier.com/locate/tws

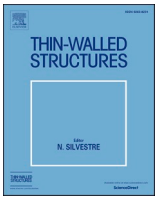

Full length article

Experimental and numerical characterization of column webs/faces loaded out-of-plane in steel joints

Melaku Seyoum Lemma [a,*], Carlos Rebelo [a], Jorge Conde Conde [b], Luís Simões da Silva [a]

[a] Civil Engineering Department, ISISE, ARISE, University of Coimbra, Portugal
[b] Departamento de Física y Estructuras de Edificación, Universidad Politécnica de Madrid, Spain

ARTICLE INFO

Keywords:
Steel joints
Minor axis connection
Bolted connection
Face plate component
Initial stiffness

ABSTRACT

This paper presents a comprehensive investigation into the behavior of column webs/faces under out-of-plane loading within steel joints. The experimental component of the study involves testing five profiles, encompassing both open and closed sections with varying web slenderness and steel grade, subjected to direct out-of-plane tensile loads through bolted connections, utilizing both single and double rows of bolts. Concurrently, numerical simulations are conducted using finite element models, thoroughly calibrated with the experimental results. Drawing upon the calibrated numerical models, the paper systematically explores the influence of key parameters, including web slenderness, bolt arrangement, and analysis methods, through a parametric study involving 167 cases. A careful comparison of the observed behavior of the component from experimental tests, numerical models, and analytical models for initial stiffness is presented. Finally, the initial stiffness formulation derived from a recent model developed by the authors is improved to align with the observations from the experimental and numerical results.

1. Introduction

It is established in the literature that beam-to-column connections to the minor axis of an I/H column or to the faces of tubular columns are often classified as partial strength and semi-rigid connections. Janss et al. [1] contributed to this understanding through an experimental investigation of minor axis and 3-D joints, wherein the semi-rigid behavior of the minor axis end plate, double web cleat, and flange cleat connections was observed. Packer et al. [2] built upon this knowledge by conducting 11 tests and proposing design methodologies for welded connections. Lima et al. [3] contributed with a mechanical model aligned with the Eurocode approach, derived from their experimental work. Further investigations by Chin et al. [4] explored 18 extended end-plate and flush end-plate connections to the column web with and without strengthening from backing plates and stiffeners. Kim et al. [5] studied the structural performance of welded and bolted split tee, end-plate, and bracket-type minor-axis connections to H-profiles through an experimental campaign. Dabaon et al. [6] tested minor axis and spatial joints with bare steel and composite beams and highlighted the influence of interactions. More recently, Gao et al. [7] studied minor axis joints in an exterior column using stainless steel. In parallel investigations, Pan et al. [8] and Chen et al. [9] experimentally studied flush end-plate and web and seat cleat connections attached to the column web. Tahir et al. [10] investigated such connections in a numerical study.

In the case of tubular columns, Korol and Ghobarah [11] conducted tests on five endplate connection specimens connecting W-beams to square tubular columns. Wang [12] performed a similar study focusing on determining the yield strength of blind-bolted (hollo bolt) connections to SHS (Square Hollow Section) using 11 test samples. Furthermore, Garcia et al. [13–15] conducted experiments involving I-beam to RHS (Rectangular Hollow Section) column connections utilizing angle cleats and welded studs. Throughout these investigations, the observed behavior of the joints consistently aligns with typical semi-rigid characteristics. Several authors recommend the incorporation of considerations for the resistance and rotation capacity of these joints in the design process.

In both cases, webs of I-section columns or faces of tubular columns, all the above investigations highlighted the major role of the out-of-plane response of the web/face in the global behavior of these joints [16]. Regarding the characterization of the column web behavior under out-of-plane loads, Neves et al. [17,18] proposed models for the initial, secant, and post-yield stiffness using an equivalent strip model of the

* Corresponding author.
E-mail address: melaku.seyoum@uc.pt (M. Seyoum Lemma).

https://doi.org/10.1016/j.tws.2024.112141
Received 29 January 2024; Received in revised form 13 April 2024; Accepted 14 June 2024
Available online 15 June 2024
0263-8231/© 2024 The Authors. Published by Elsevier Ltd. This is an open access article under the CC BY-NC license (http://creativecommons.org/licenses/by-nc/4.0/).

Nomenclature

a	weld throat thickness
b_c	chord width of tubular section
b_{clear}	clear depth of the web or chord
b_f	flange width of profile/section
c	vertical distance between washer edges
d	horizontal distance between washer edges on the same bolt row
d_m	mean of the across points and across flats dimensions of the bolt head or the nut
d_w	clear depth of the web
d_{washer}	washer diameter
E	young's modulus
F	force
F_{memb}	membrane force
f_u	ultimate strength of material
f_y	yield strength of material
G	shear modulus of material
h *or* h_c	height of profile/section
L_{sp}	length of specimen
p	distance between bolt rows
r_c	root radius of I-section
r_i	inner radius of tubular section corners
r_o	outer radius of tubular section corners
S_{ini}	initial stiffness
t_f *or* t_{fc}	flange thickness
t_w *or* t	web thickness
U	boundary condition for support displacement
W	distance between bolt columns
AVG	average
COV	coefficient of variation
DIC	digital image correlation
LVDT	linear velocity displacement transducer
PEEQ	equivalent plastic strain
RMSE	root mean square error
α	bolt row spacing to web width ratio
β	bolt horizontal spacing to web width ratio
δ_{web}	web out-of-plane geometric imperfection
Δ	displacement
ε	strain
ε_u	ultimate strain
μ	web slenderness: web width to thickness ratio
ν	poisson's ratio
θ	boundary condition for support rotation
σ	stress
ζ	single bolt row height to web width ratio

web. Lima et al. [3] subsequently extended the applicability of this model to account for stiffener effects on the connection behavior. Silva et al. [19] have demonstrated the model's suitability for connections to tubular columns. Park et al. [20,21] proposed a formulation for the initial stiffness of the face in tension on a row-by-row basis, solving the equation for plate deformation under transverse load. Ye et al. [22] derived equations to calculate the bending stiffness of the SHS/RHS column face through a regression analysis on a database of numerical results. More recently, Conde et al. [23] proposed a novel approach, approximating the plate problem through an equivalent grid of beams on an elastic foundation.

Meanwhile, the guidelines for the design of joints provided in part 1–8 of both EN1993 (2005) [24] and FprEN1993 (2023) [25] mainly focus on major axis joints, resulting in an absence of specific directives for the design of semi-rigid bolted joints in the minor axis of open sections and bolted connections to tubular columns. Existing analytical models for assessing the stiffness of the column web/face under out-of-plane bending are constrained to ranges of application. Similarly, formulations for the resistance, usually based on yield-line theory, exhibit significant variability, generating disparate estimates. Hence, there is a need for comprehensive and reliable models to systematically characterize the behavior of the column web/face under out-of-plane loading (hereinafter referred to as face plate component) across diverse joint configurations.

The main objective of this study is to address this gap by undertaking a comprehensive investigation, encompassing both experimental and numerical approaches, into the behavior of the face plate component under out-of-plane loading. To provide a comprehensive overview, the paper initially presents key aspects of the experimental campaign [26], including the test setup, instrumentation details, and ancillary data collection procedures. Subsequently, the findings of the experiments are detailed. Then the development and calibration of advanced finite element models (FEM) is discussed. Based on the calibrated numerical models, the paper discusses the influence of various parameters, such as web slenderness, bolt arrangement, and analysis methods on the web/face behavior through a parametric study. Finally, the test and finite element analysis (FEA) results are compared against available formulations for the estimation of initial stiffness of this component, and an improvement of the Conde model is proposed.

2. Experimental program overview

The experimental campaign is focused on studying the webs of column specimens subjected to direct out-of-plane tensile load through connections that include single and double rows of M24 – 10.9 bolts with three distinct bolt arrangements. Detailed descriptions of the specimens tested, the testing layout, and the instrumentation utilized are presented in the subsequent sections.

2.1. Experimental setup and layout

The experimental setup comprises a reaction frame, which supports the specimens, and a reaction wall that supports the hydraulic actuator. As illustrated in Fig. 1, the reaction frame is constrained against deformations in the loading direction by two bracing struts positioned at the top and bottom reaction beams. The test specimens are placed vertically between the top and bottom hinges, enabling the specimen ends to rotate freely around a horizontal axis that is parallel to the specimen web. The load was transferred to the web through a set of connectors specifically designed for this purpose, extending from the actuator tip to the specimens' webs. These connectors featured three distinct perforations to accommodate the three different bolt arrangements utilized in the experimental tests. To ensure a successful transfer of the load to the web, the remaining part of the connection, i.e., the connector pieces and the bolted connections, were over-designed to have reserve strength until failure occurred in the web specimen. A displacement-controlled test protocol was adopted where an imposed displacement was applied through the actuator at a constant rate of 0.01 mm/s until either the maximum load capacity was reached, or the specimen failed.

2.2. Specimens

It is already established in the literature that the column web panel behavior largely depends on the column web width to thickness ratio and the geometric ratios of the bolt pitch and gage distances to the web

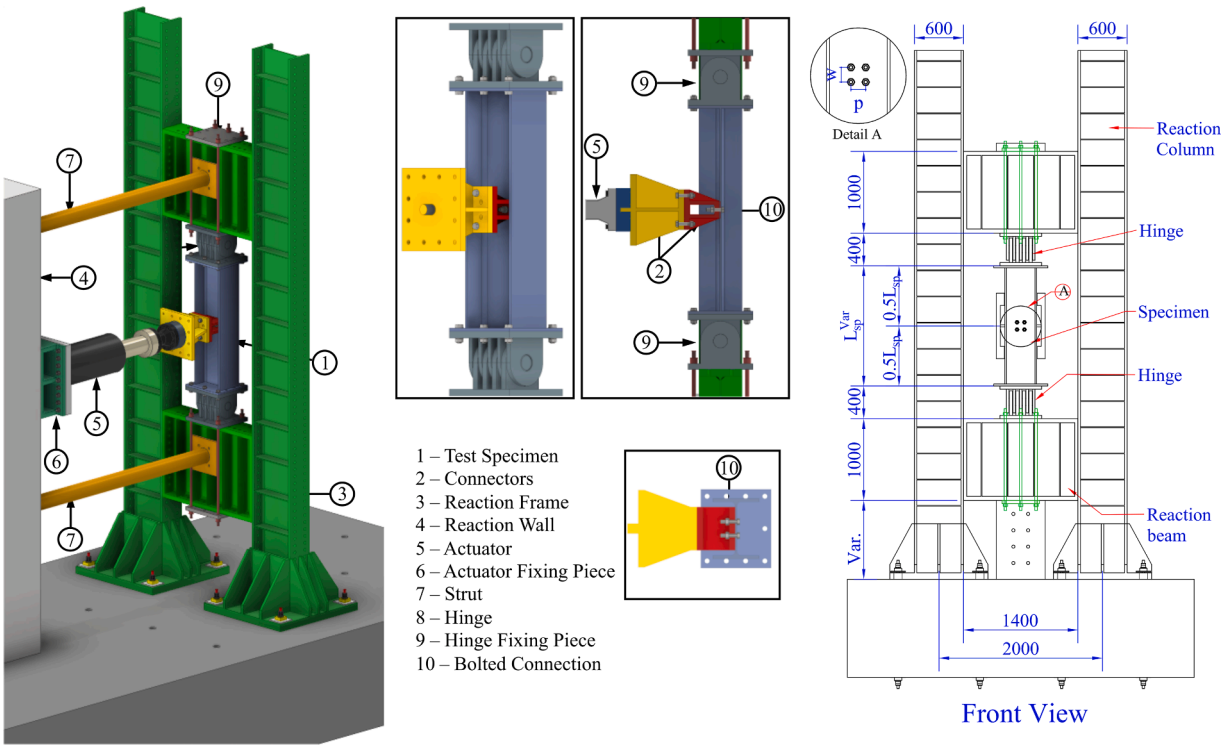

Fig. 1. 3D schematic of the test setup & details [units: mm].

Table 1
Description of the specimens and their nominal dimensions.

Profile	d_w [mm]	μ (d_w/t_w)	Length [mm]	Steel Grade	Bolt Rows	Bolt Spacing [mm]	
						W	P
HEA400	298	*27.1*	1430	S460	1	–	90
HEB400	298	*22.1*	1750	S275	2	90	165
HEB600	486	*31.4*	1910	S355	2	90	200
Girder750 × 200	705	*88.2*	1465	S690	2	90	200
SHS200 × 10	156	*15.6*	1700	S355	1	–	90

width. Therefore, the conducted tests encompassed five distinct profiles with varying web slenderness and steel grades indicated in Table 1, comprising both open and closed sections (Fig. 2). Among the profiles tested were three hot-rolled H-sections, whose web slenderness ranged between 20 and 35. These profiles were selected because about 37 % of the commercial European HE profiles lie in this web slenderness range.

Furthermore, the unique flange width (300 mm) in the first three specimens with variable flange thickness was considered an advantage as it yields variable support fixity to the column webs. Additionally, a high-strength steel (S690) welded plate girder, featuring a large web slenderness of 88, was also included. Recognizing the significance and consequential impact of out-of-plane loading on the face of tubular sections, an SHS200 × 10 square hollow section was also tested.

2.3. Instrumentation

The deformation of the specimens, the connecting parts, and the supporting reaction frame were monitored using 34 linear variable differential transformers (LVDTs) and laser displacement sensors. Two-thirds of these sensors were dedicated to tracking the deformation of the specimens while the remaining controlled the displacements on the supporting structures. Deformations of the specimens' webs and flanges in the loading direction were measured by LVDTs positioned at intervals of one-quarter of the specimen length along its length (Figs. 3 and 4). Moreover, 4 LVDTs were used to track the opening and closing of the flanges at the central load application zone due to the out-of-plane load. Linear strain gauges and rosettes were systematically placed on the reverse side of the loaded web, based on information obtained from the pre-test preliminary numerical simulations. Most of the strain gauges were placed in the region where theoretical yield lines are expected, obtained from the log-spiral fan yield-line model developed by Gomes [27]. In addition, the top and bottom-most rows of the strain gauges were placed outside this region to track yield propagation. The applied loads were read from a load cell within the actuator that was calibrated for tensile forces up to 1000 kN. Each test employed a total of 46–58 channels of instrumentation.

The study employed a DANTEC Q400 Digital Image Correlation system (DIC). Contrasting speckles were applied to the web facing the cameras by first painting the specimens white and later carefully sprinkling/spraying black dots using a paint gun. The DIC system (Fig. 5) captured images of the specimen from two angles, allowing for the computation of spatial deformations. Before each test, the system was calibrated using calibration checkerboards and the cameras' positions, and the illumination was adjusted to achieve high correlation accuracy. The collected data, generally sampled at 1–2 Hz frequency, was post-processed by the ISTRA4D computer program to provide the correlation that gives spatial deformations relative to the initial state.

2.4. Material properties

The five specimens were of different material grades ranging from S275 to S690. In the scope of this research, the material properties of the profiles and bolts tested were assessed through a series of coupon tests according to ISO 6892–1[28]. In the column profiles, coupon samples

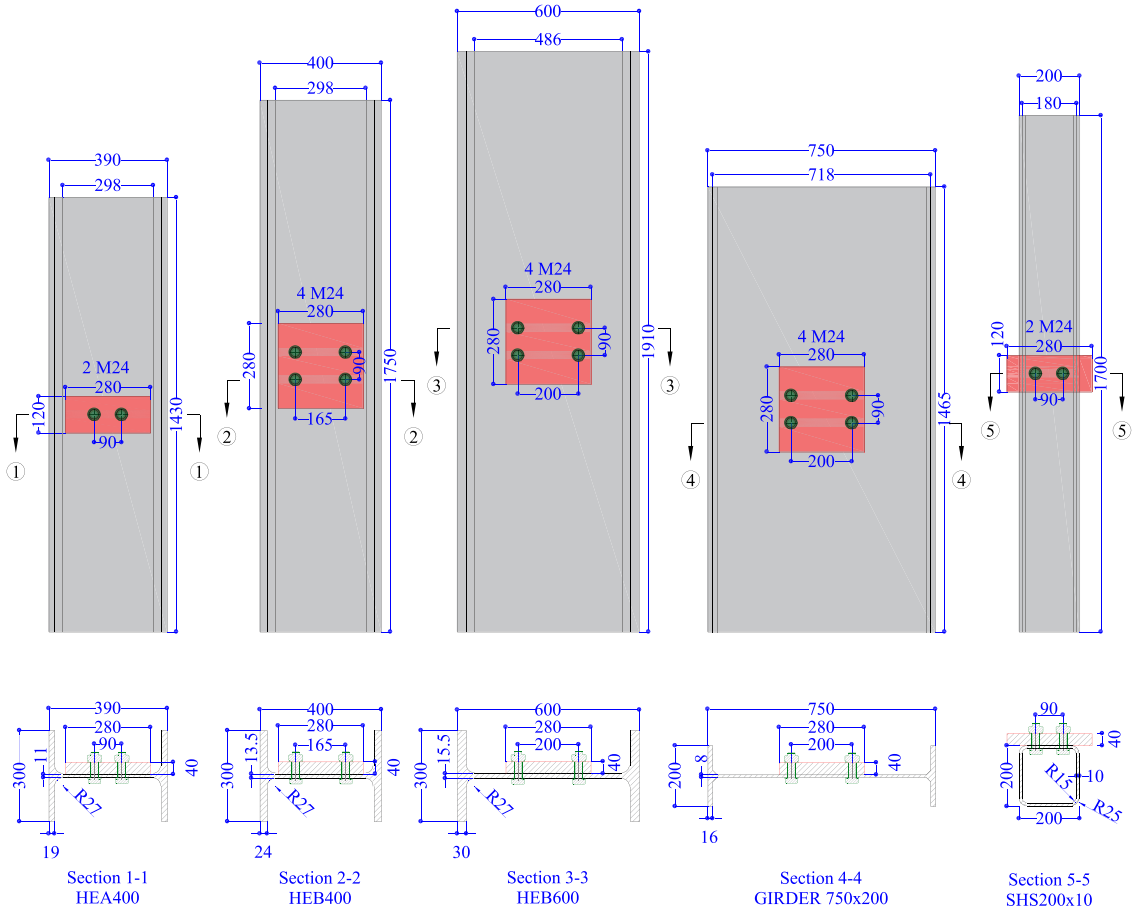

Fig. 2. Specimen dimensions and connection details.

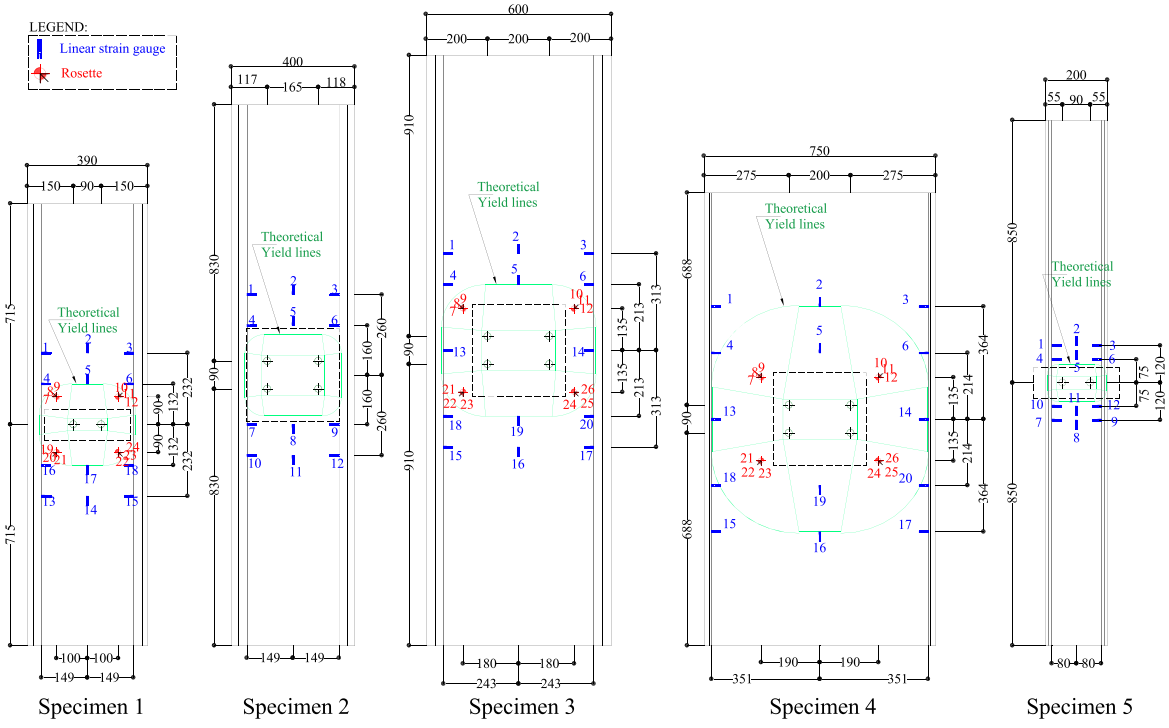

Fig. 3. Specimens Instrumentation – Strain gauges.

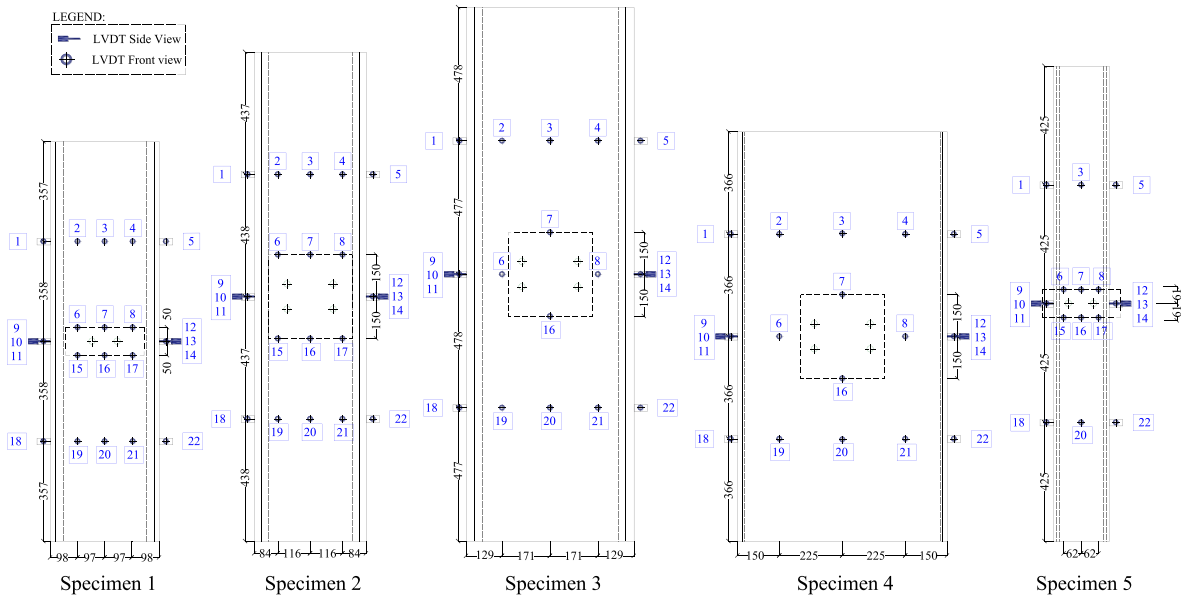

Fig. 4. Specimens Instrumentation – LVDTs.

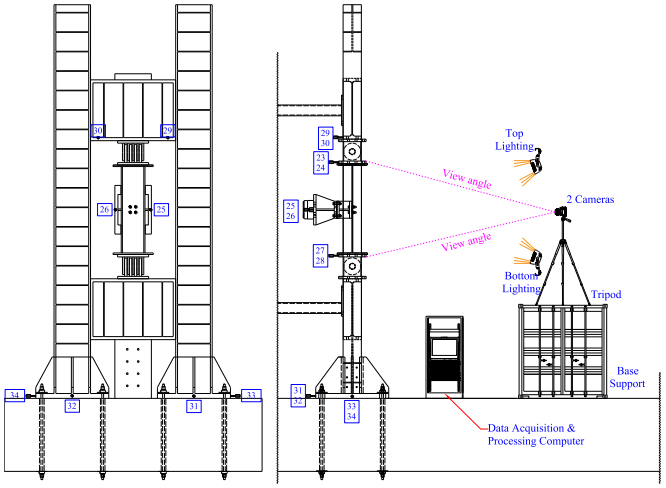

Fig. 5. Support Instrumentation & DIC Setup.

were extracted from the webs where the specimens were expected to sustain higher stresses. Whenever possible, these samples were taken in the rolling, transverse, and diagonal directions. The bolts coupon samples, on the other hand, were machined from the shank into the shape depicted in Fig. 16.

From the coupons in the three directions, slightly higher resistance was generally observed for the coupons in the rolling direction. Table 2 summarizes the relevant mechanical properties determined from the tests, i.e., the elastic modulus, yield strength, and ultimate strength, from the coupons extracted in the transverse direction. The corresponding engineering stress-strain curves are shown in Fig. 17 in Section 4.1.1 together with their numerical calibration. It is noted that, as expected, the best matches in the numerical models were obtained using the properties in the transverse direction.

Table 2
Mechanical properties of the materials.

Material	E[GPa]	f_y [MPa]	f_u[MPa]	e_u[%]	f_u/f_y[-]
HEA400	202.51	483.28	555.79	15.33	1.15
HEB400	210.60	377.67	475.86	19.19	1.26
HEB600	174.04	414.59	510.31	16.26	1.23
Girder	205.05	760.89	818.38	7.17	1.08
SHS200 × 10	213.75	438.45	574.22	17.02	1.31
M24 Bolts	230.60	1067.68	1167.59	4.37	1.09

2.5. Initial geometric imperfections

Before testing, a measurement of the initial geometric imperfections in the specimen profiles was made using an ATOS-Q 3D laser scanner. A beam of laser light was projected from the scanner onto the specimen surface (Fig. 6a) and several images were taken using two cameras progressively moving along the length of the specimen/section. The point clouds generated from the scanning were triangulated and the resulting mesh (Fig. 6b) was overlaid on the ideal geometric models of the profiles for 3D inspection to determine the locations and magnitudes of the deviations/imperfections.

Surface comparisons were made between the scanned meshes (actual dimensions) and their respective profiles with 'ideal' geometries (nominal dimensions) to highlight the magnitude and distribution of initial geometric imperfections as shown in Fig. 7. The deviations were checked and verified against the essential tolerances in EN1090–2 [29] for web plate (i) curvature (b/200), undulation (b/100), and distortion (b/100), where b is the plate width.

In general, the overall imperfections along the members were small ($< L_{sp}$/1500, where L_{sp} is the specimen length). A summary of the geometric imperfections obtained from the scans is presented in Table 3. The table shows the deviations in profile dimensions at the cross-sectional level from their nominal values (in parenthesis) averaged over the region where the bolted connections were formed later and the amplitude of the out-of-plane initial imperfection in the web.

3. Test observations and discussion

3.1. Displacement computations

The total displacement measured by the LVDTs consisted of deformations of the column web, bending deformation of the column, deformations in the reaction frame, and small deformations between bolted connections of the jack and the connectors. To identify the origins

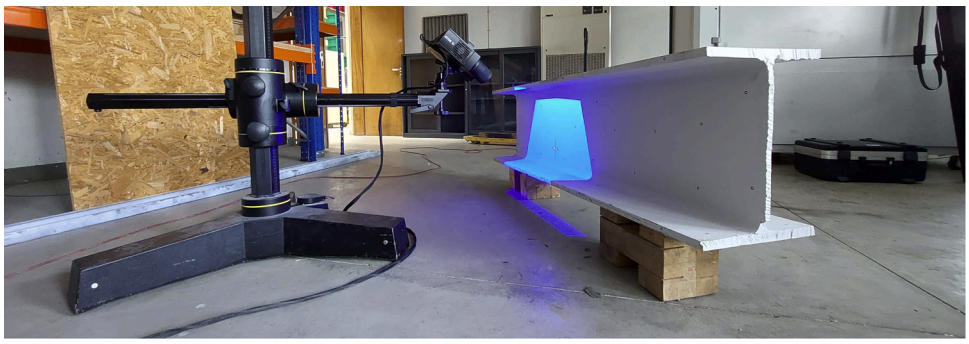

(a) Scanning

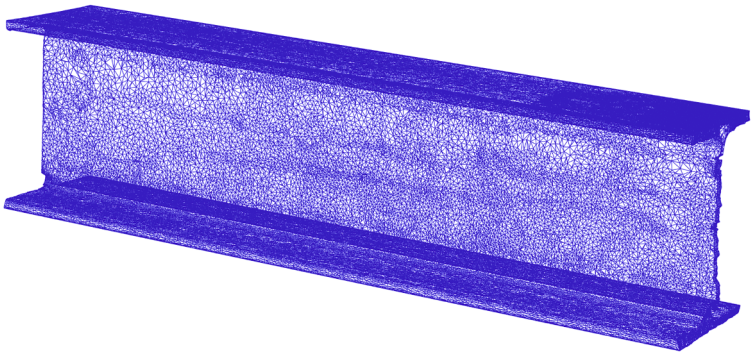

(b) Mesh Triangulation

Fig. 6. 3D Scanning of a specimen.

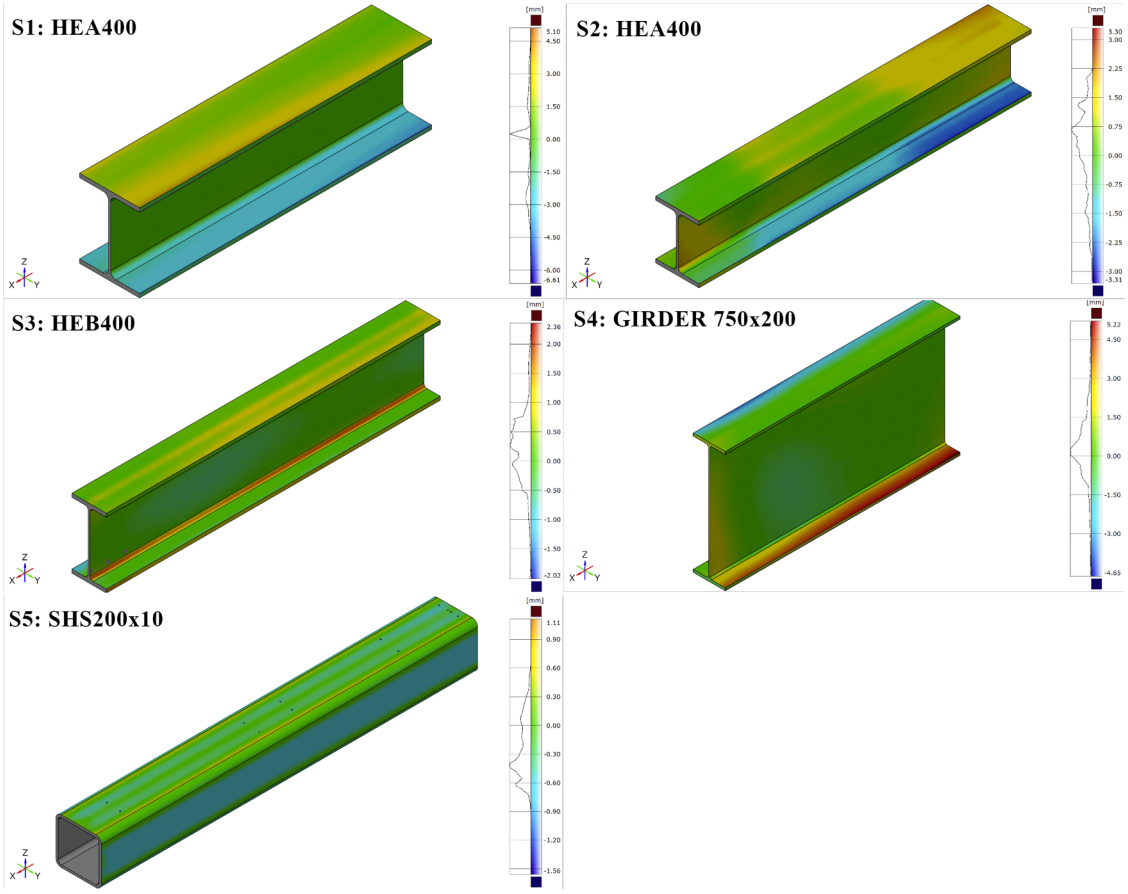

Fig. 7. Initial Geometric Imperfections.

Table 3
As measured cross-section properties with imperfections [units: mm].

Profile	h	t_f	t_w	r_c / r_i / r_o / a	d_w	δ_{web}
HEA400	395 (390)	19 (19)	11.5 (11.0)	25.5 (27)	306 (298)	0.15
HEB400	402 (400)	24.5 (25)	14.25 (13.5)	26.25 (27)	300.5 (298)	0.23
HEB600	601.4 (600)	30.25 (30)	15.83 (15.5)	25.5 (27)	480.96 (486)	0.61
Girder750 × 200	748 (750)	15.8 (16)	8.33 (8.0)	7.92 (a:7.0)	694.6 (705)	1.01
SHS200 × 10	200	10	10	26.85, 17.15 (r_o 25, r_i 15)	146.3	0.10* 0.44**

* front loaded chord of the tube.
** side chords of the tube.

of the small deformations that may occur on the loading elements side of the layout, reference can be made to Figs. 1 and 5. The total displacement was determined from LVDTs which were placed just in front of the actuator at the back of connector 1. This way, the deformations coming from the actuator side were safely disregarded. In conjunction with these readings, the displacement at the center of the bolt group read by DIC was tracked to check the data accuracy.

$$\Delta_{tot} = \Delta_{web} + \Delta_{column} + \Delta_{frame} + \Delta_{others} \quad (1)$$

$$\Delta_{others} = \Delta_{bolt} + \Delta_{c1-c2} + \Delta_{actuator-c1} + \Delta_{dywidag} \quad (2)$$

Other sources included gap openings between the actuator end and connector 1, as well as between connectors 1 and 2. However, it should be noted that these deformations are expected to be small, as these connections were much stronger than the tested connections, given their size and the high number of bolts used. Disregarding these sources, one is left with the deformation at the bolt-web interface $\Delta_{connection}$ which represents displacements arising from phenomena such as bolts punching through the plate, indentation of the washers, and thread stripping. The equations for total deformation become:

$$\Delta_{tot(L25,L26)} = \Delta_{web} + \Delta_{col} + \Delta_{frame} + \Delta_{connections} \quad (3)$$

$$\Delta_{tot(DIC)} = \Delta_{web.dic} + \Delta_{col.dic} + \Delta_{frame} \quad (4)$$

An exaggerated deformed shape of the specimen is shown schematically in Fig. 8. The faded hidden lines indicate the original position and form, while the solid lines show the deformed state. To isolate and compute the deformations in the web alone, the equations above can be rearranged as:

$$\Delta_{web.cen} = \Delta_{tot.cen} - \Delta_{col.cen} - \Delta_{frame.cen} - \Delta_{connections} \quad (5)$$

Or using the DIC readings,

$$\Delta_{web.cen} \cong \Delta_{tot.dic.cen} - \Delta_{col.dic.cen} - \Delta_{frame.cen} \quad (6)$$

This equation will be henceforth used.

3.2. Load-deformation and DIC observations

The force-displacement plots for the five specimens are presented in Fig. 9. The deformations of the web surface extracted from DIC for four different load levels are also presented in Fig. 9. It can be observed from the figures that most of the deformation occurred in the connection

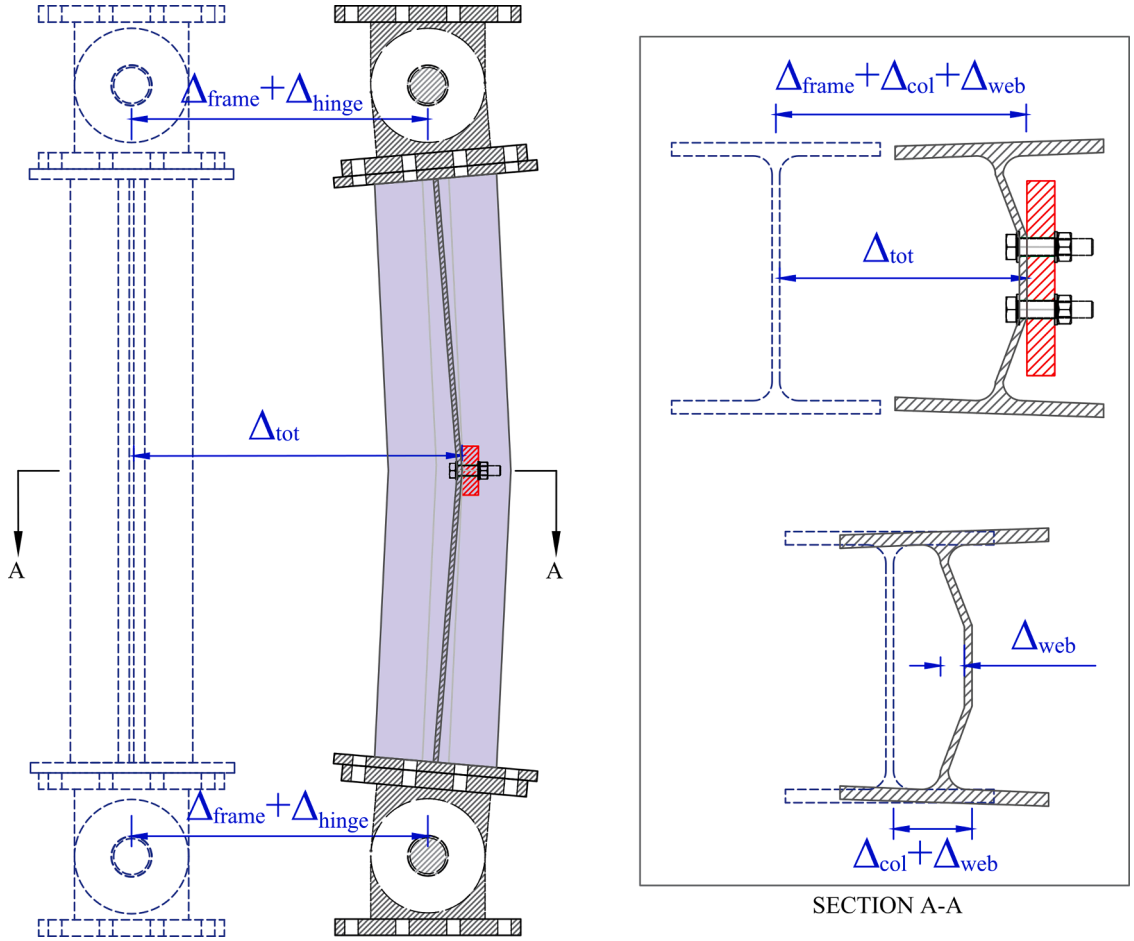

Fig. 8. Exaggerated schematic drawing of the specimen and support deformations.

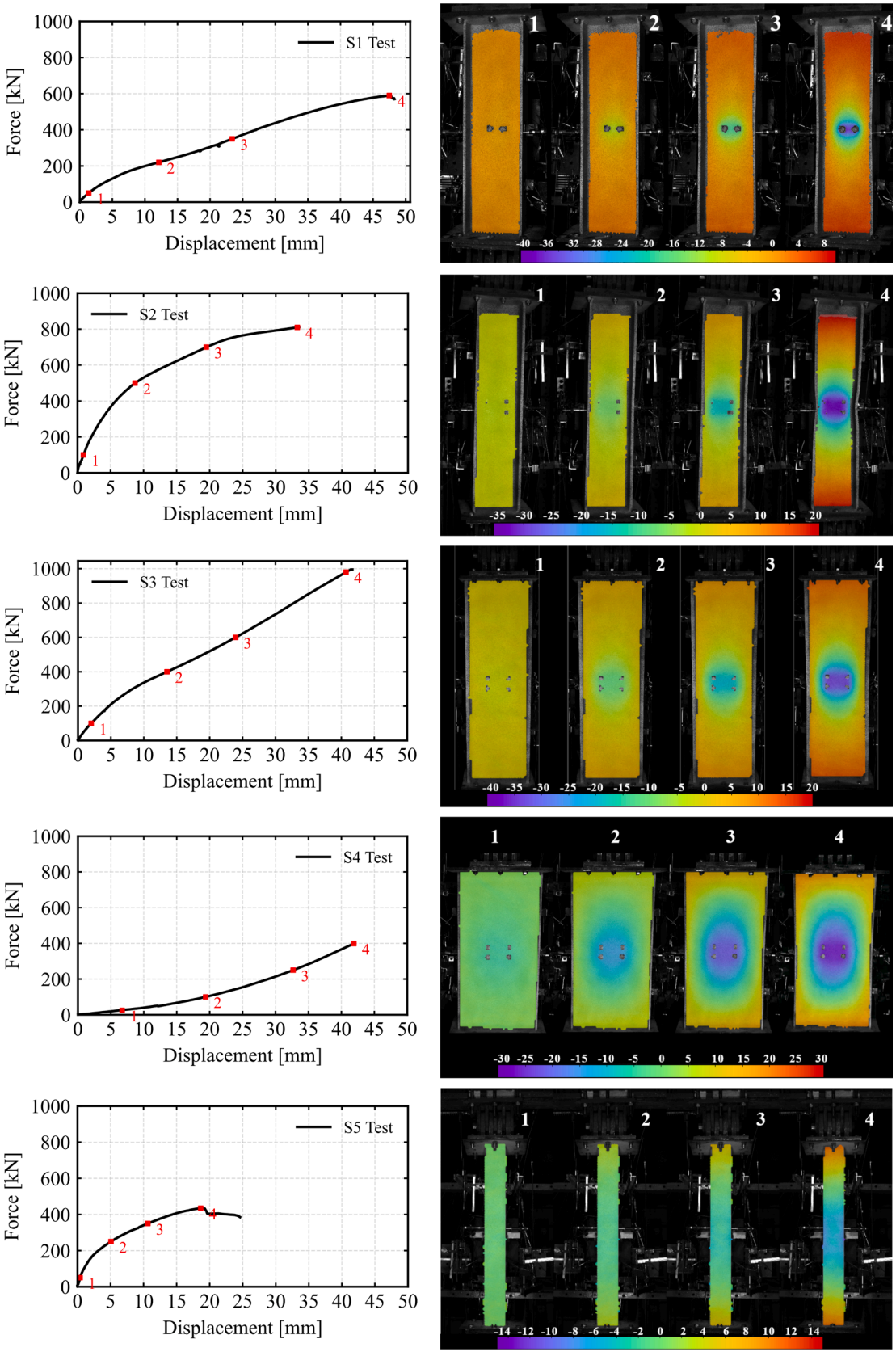

Fig. 9. Force-Displacement plots & web surface displacements from DIC.

region. In addition, the local deformation in the flanges is also apparent.

A similar behavior is noticed for all test specimens, except for the plate girder. The plots show three distinct regions, each with different behaviors. The first region is the initial zone, where stiffness is high. As the loading is increased and the web yields, the stiffness starts to show a significant reduction. This is followed by a portion of the curve (short in some tests and longer in others) where the post-yield stiffness remains constant. After the initial post-yield stiffness, there is either (i) a rapid increase in stiffness, indicating the onset of the second post-limit stiffness, where membrane actions become dominant or (ii) a decline in stiffness following plastification of the section including the supporting flanges.

In the case of the welded girder (S4) which features a slender web, the initial response dominated by the web bending results in a low initial stiffness. As loading increases, membrane forces become dominant, and a substantial increase in the stiffness is witnessed in the later phase. Although not reached in the test, a further increase in loading would result in the web plate yielding in combined tension and flexure and the stiffness declining.

3.3. Strain response

The strain gauges were positioned exclusively on the back face of the web, which was on the loading actuator's side. As a result, for the case of pure bending, the strains at the level of the bolt group were expected to be (i) compressive for the horizontally placed strain gauges at the bends/kinks near the root radius, (ii) tensile at the horizontal and vertical bends near the edge bolts and (iii) compressive for the vertically placed strain gauges in the region where the web kinks in the vertical direction as illustrated in Fig. 10.

Fig. 11 presents the strain responses recorded during the tests, categorized by the location and orientation of the strain gauges. The horizontal components of the rosettes detected tensile strains as the web plate was pulled away from the flanges within the radial fan where the rosettes were positioned. In contrast, the remaining strain gauges consistently recorded compressive strains throughout the tests for the first three specimens. However, the compressive nature of these strains reversed when the tensile forces resulting from membrane actions exceeded the compressive stresses arising from the bending of the web plate. The force-displacement plot for the first three specimens reveals a noticeable correlation between the points of strain reversal and the commencement of the second post-yield range, where membrane effects dominate. In specimen 4, while the edge strain gauges registered compressive strains, all the remaining strain gauges indicated tensile strains, indicating the presence of active tensile stresses elsewhere across the web. Notably, deviating from the observed patterns in other specimens, the edge strain gauges situated at the edges of the flat face were exclusively under tension for the tubular column.

There is some asymmetry in the strain response, especially in the first and last specimens, which is also notable in the final deformed shapes of the specimens (Figs. 12, 15). This asymmetry is primarily due to slight

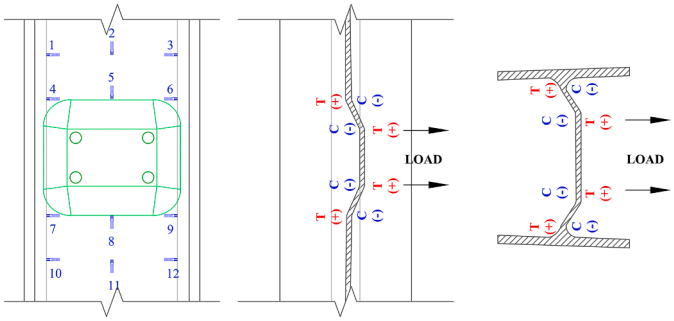

Fig. 10. Strain senses on the two faces of the web in bending.

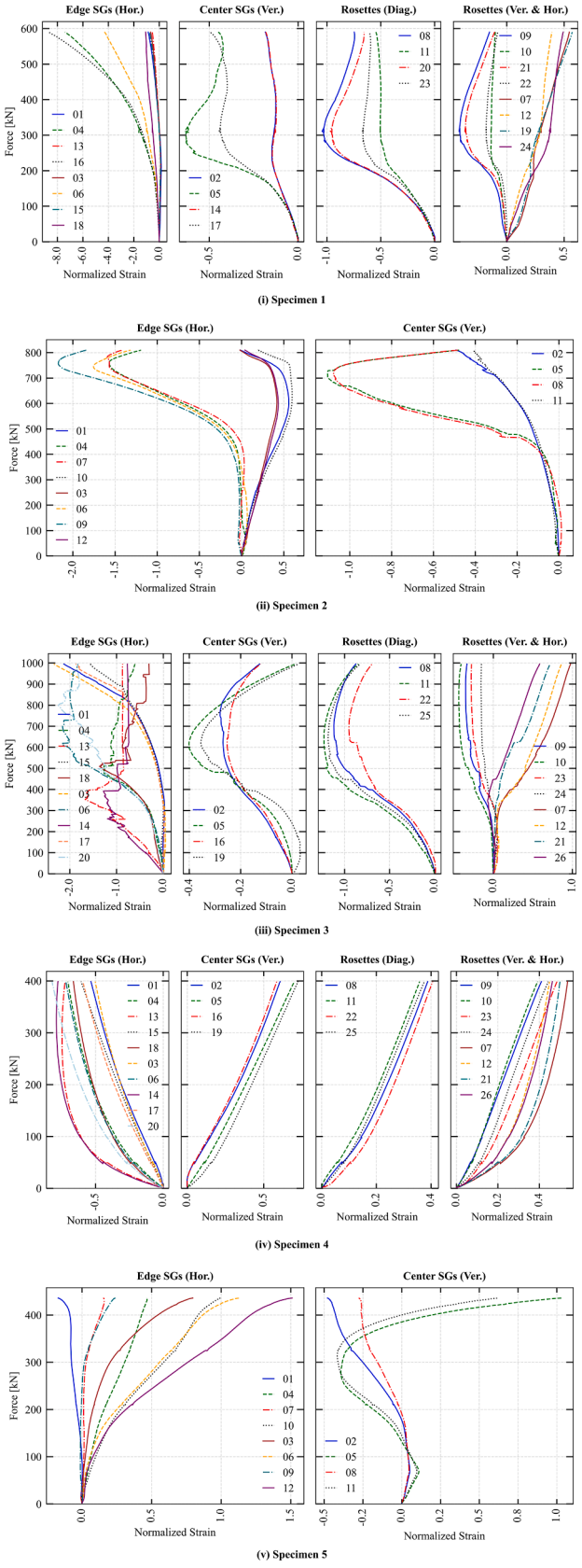

Fig. 11. Strain progressions with applied force.

eccentricities during load application. However, these effects do not impact the results, as later numerical simulations have confirmed.

3.4. Plastic deformation and failure mechanisms

The failure modes observed in the single bolt row specimens involve excessive deformation at the bolt-hole region, with punching failure observed for the tubular section. In contrast, for the two bolt row cases, yielding of the loaded region (bolt group) with radial fan-shaped yield lines is observed. In these cases, the free-to-deform flanges undergo significantly increased yielding, especially after the web yields. The flanges on the loaded face open while those on the opposite face close. Most of the yielding occurs on the compressed flanges that ultimately buckle inward locally. In this section, the discussion regarding specimen yielding inferred from the observed paint disintegration, was validated through two methods: (i) readings from strain gauges at critical locations and (ii) subsequent confirmation through calibrated numerical simulations (refer to Section 4.2.3).

Fig. 12 illustrates the plastically deformed state of specimen 1 at the end of the test. This specimen, which featured a single-bolt-row connection, exhibited high local deformations at the bolt holes. As a result, yielding was primarily concentrated in this region. Layers of paint broke and peeled off near the web edges where yielding occurred near the root radius. The bolts protruded through the web, leading to bolt-hole deformations that resemble truncated hyperbolic cones. The washers also sustained significant indentations and, in some cases, even fracture. Nevertheless, the failure mode of specimen 1 was the detachment of the bolts from the connector pieces due to thread stripping of both nuts and bolts. The flange deformation was generally small but signs of yielding on the outer face of the compression side were apparent.

Similar observations are made for specimen 2. Yielding around the bolt-hole circumference is relatively weaker as compared to the first specimen. Yet, minor radial ripping-type cracks were seen around each bolt hole. Since the load was applied over a wider area impounded by the bolt group, it mobilized the deformation of a larger portion of the flanges. Fig. 13 shows that the inward buckling of the flanges on the compression side was particularly larger/accentuated. Consequently,

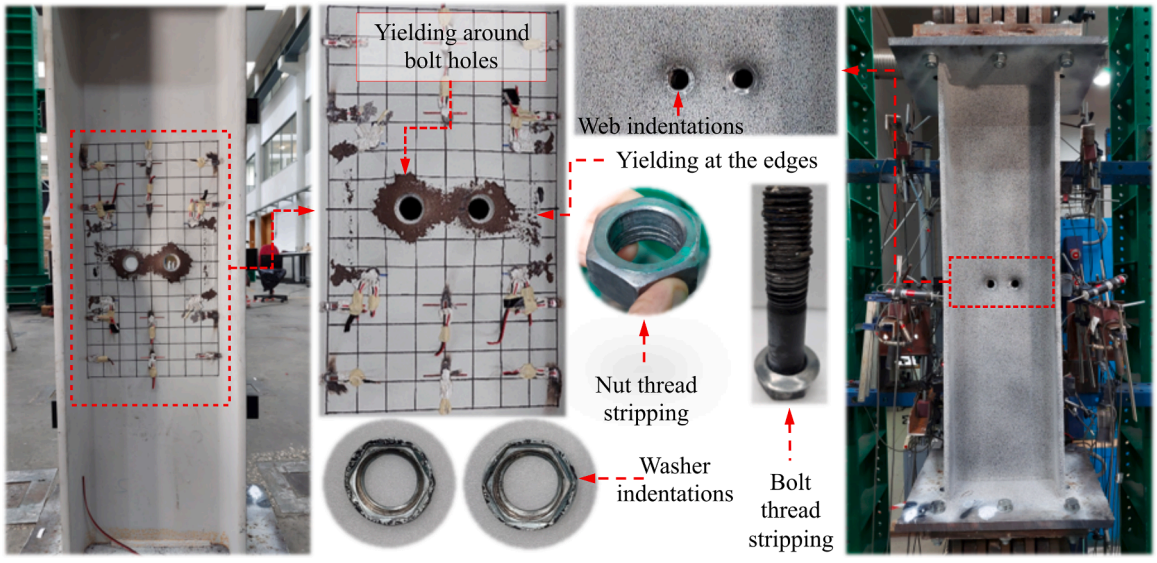

Fig. 12. Specimen 1 - deformations at the end of the test.

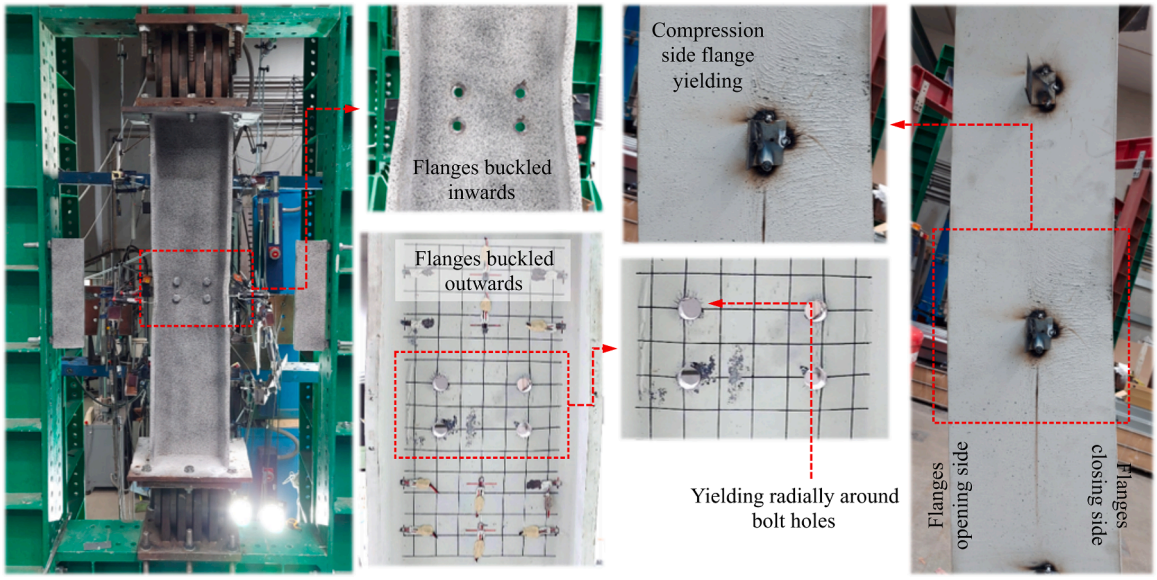

Fig. 13. Specimen 2 - deformations at the end of the test.

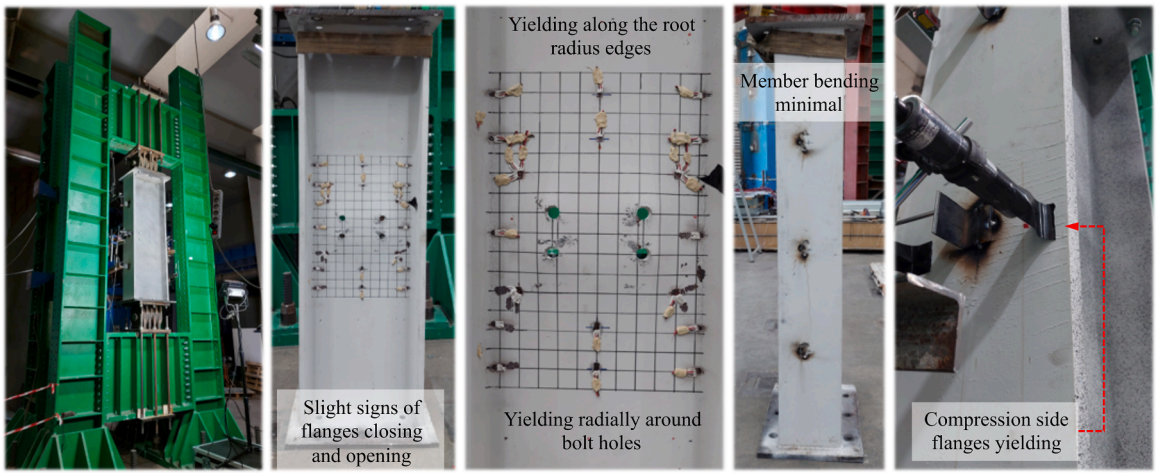

Fig. 14. Specimen 3 - deformations at the end of the test.

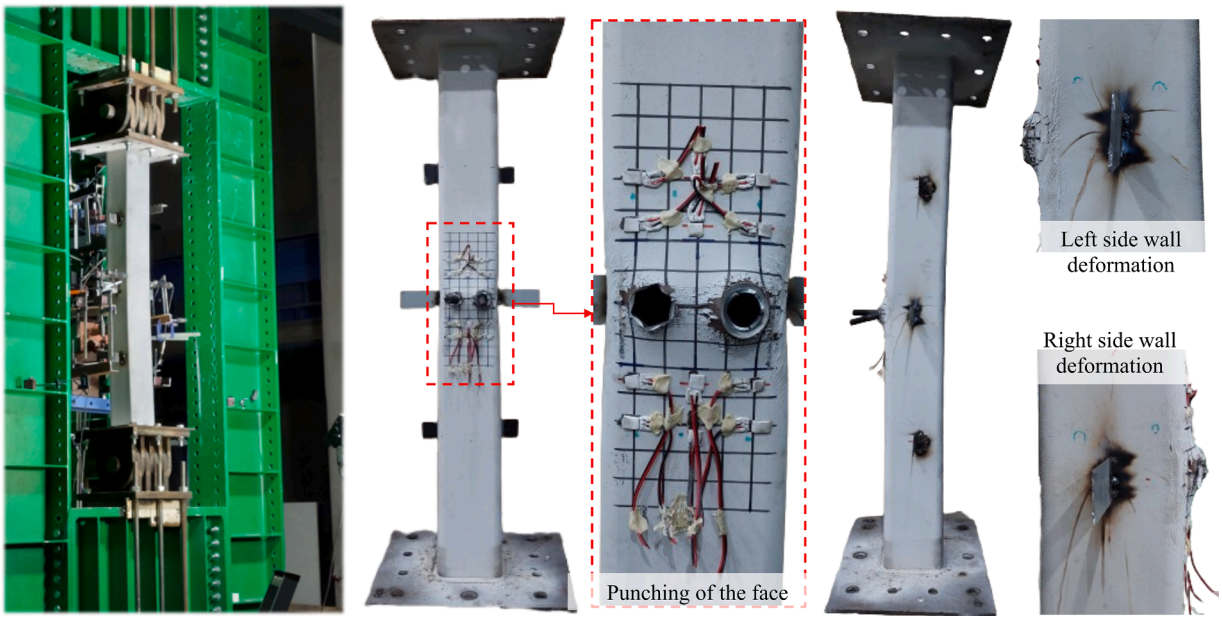

Fig. 15. Specimen 5 - deformations at the end of the test.

clear signs of yielding on the outside surface of the flanges were visible. As can be noticed from the force-displacement plot for this specimen (Fig. 9), the final stage of the test is characterized by almost "zero" stiffness. Deformations beyond a net web displacement of about 25 mm were accompanied by repeated creaking coming from the hinges. The test was stopped after an additional 10 mm displacement load was applied under the said circumstances before eventual plastification of the whole section about the minor axis.

There was no apparent failure mode for specimen 3 as the test continued until the load cell's limit (1000 kN) was reached without failure. Indeed, the thicker flanges of this specimen were able to provide stiff support to the column web when compared to the other tests. Radial yielding around the bolt holes was observed, as in the other tests, as well as yielding along the root radius edges. Although the plastic opening and closing of the flanges were small, cracking of the coating/paint on the column flanges was noticed indicating yielding in the region marked in Fig. 14.

In contrast to the foregoing cases, specimen 4 featured a section with a highly slender web plate in high-strength steel. The large spacing between the load application points on the web and the lateral supports (flanges) resulted in large membrane resistance from an early stage of loading. The test was, unfortunately, interrupted due to the failure of a rod on the hinge fixing system – away from the specimen – after loading was applied only up to a net displacement of 42 mm on the web, which is not enough to lead to significant plastification of the web. As a result, no plastic deformation images are available.

The failure mode observed for specimen 5 was punching of the bolts through the loaded face of the tube (Fig. 15). In addition, the side faces of the tube in the vicinity of the loaded region sustained inward bending and stretching as the front face was pulled.

4. Numerical model calibration

4.1. Model implementation

The numerical models representing the experimental tests were developed using the general-purpose finite element method software Abaqus [30]. The purpose of conducting these numerical analyses was to validate models that would enable a reliable investigation of the strength and stiffness of the column webs or faces when they are subjected to transverse loading through parametric analyses. To achieve this goal, simulations involving material nonlinearity, geometric

nonlinearity, and imperfections (GMNIA) were conducted. Additional analyses were also made considering just material nonlinearity (MNA) to illustrate assumptions in determining the yield resistance from first-order analysis. Linear elastic (LE) and geometrically non-linear analyses (GNA) were also conducted for comparisons after calibration of the GMNIA model against the test results. General details common to all analyses are explained in the following sections.

4.1.1. Material properties

The engineering stress-strain properties obtained from standard uniaxial material tests were used to calibrate the material models for input in ABAQUS. Hence, replicate numerical models (Fig. 16) of the actual coupons were developed and calibrated such that material definitions were possible in a multi-axial stress state. The engineering stress-strain plots obtained from the tests and the corresponding plot from the calibrated material models are shown in Fig. 17.

The engineering stress-strain relations were converted to their true stress-strain equivalent before feeding the data to Abaqus.

$$\sigma_{true} = \sigma_{eng}\left(\varepsilon_{eng}+1\right); \varepsilon_{true} = \ln\left(\varepsilon_{eng}+1\right) \tag{7}$$

Parts of the curve beyond the ultimate strength were also considered to model strain softening and material damage. The post-necking behavior of each material was implemented in the models using the ductile damage feature in Abaqus to capture material softening and fracture. The stress-strain relation beyond the necking initiation was expressed by the combined linear and power stress-strain law [31] and calibrated to match the coupon test results. The damage initiation plastic strain was calculated for different levels of stress triaxiality, and the damage evolution was specified from the point of necking until fracture where element removal would initiate when needed.

The full-range non-linear material properties shown in Fig. 17 are used in all material non-linear analyses (MNA & GMNIA).

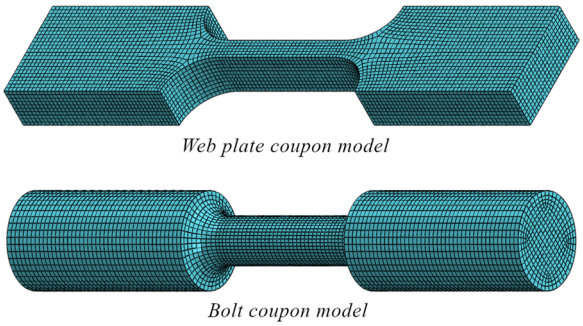

Fig. 16. Column and bolt coupons FE models for calibration.

4.1.2. Boundary conditions and interactions

Boundary conditions reflecting the conditions within the experimental setup were numerically simulated. The supporting hinges of the experimental setup were numerically simulated tying the end cross-sections of the column to constrained points located at the theoretical center of rotation (center of the hinge pins) by means of rigid links.

The bolt, washer, and nut assemblage were modelled as a single monolithic part with an equivalent unthreaded shank (see Fig. 18) with uniform material properties directly reflecting the tensile tests on the bolt coupons described above. The different parts of the test assembly, i.e., the column section, the pulling connectors/stubs, and the bolts, are in contact and therefore interact with one another. These interactions have been modeled via surface-to-surface tangential and normal contact behavior. A “hard” contact model is adopted to model pressure applied normal to interacting surfaces. Slip or sliding between the parts is modeled by a tangential behavior with a coefficient of friction equal to 0.3 [29,32,33].

4.1.3. Element type and meshing

An initial set of preliminary analyses were carried out to decide the type of solid/brick/hexahedral element to be adopted among linear and quadratic elements with different degrees of integration points, i.e., C3D8, C3D8R, C3D8I, C3D8H, C3D20, and C3D20R. In the case of the linear elements, the required number of layers through the web and flange thicknesses were also examined. For the bending-dominated problem at hand, it was observed that the models with C3D20R, C3D8R, and C3D8I performed well. With the C3D20R element type, the increase in the number of layers had only a small and insignificant effect. Therefore, 2 layers were found to give accurate enough results at a relatively lower computational requirement. Nevertheless, these

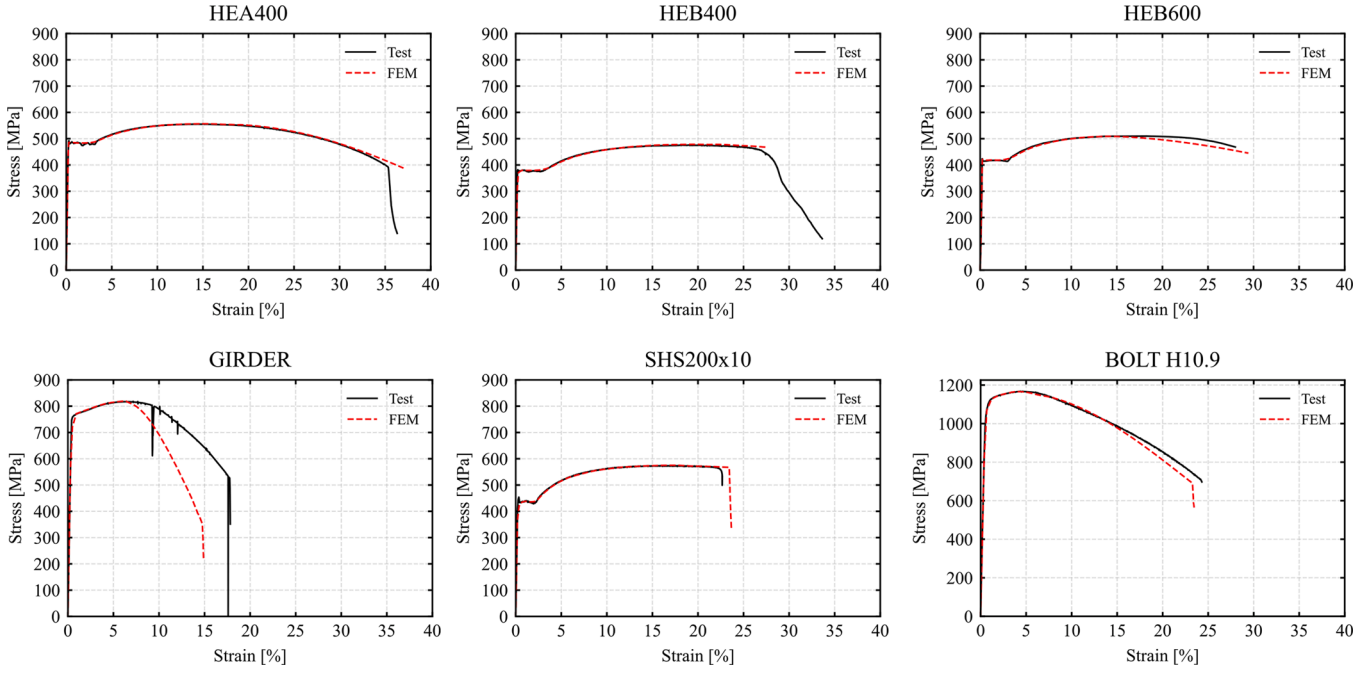

Fig. 17. Steel sections and bolt constitutive material properties.

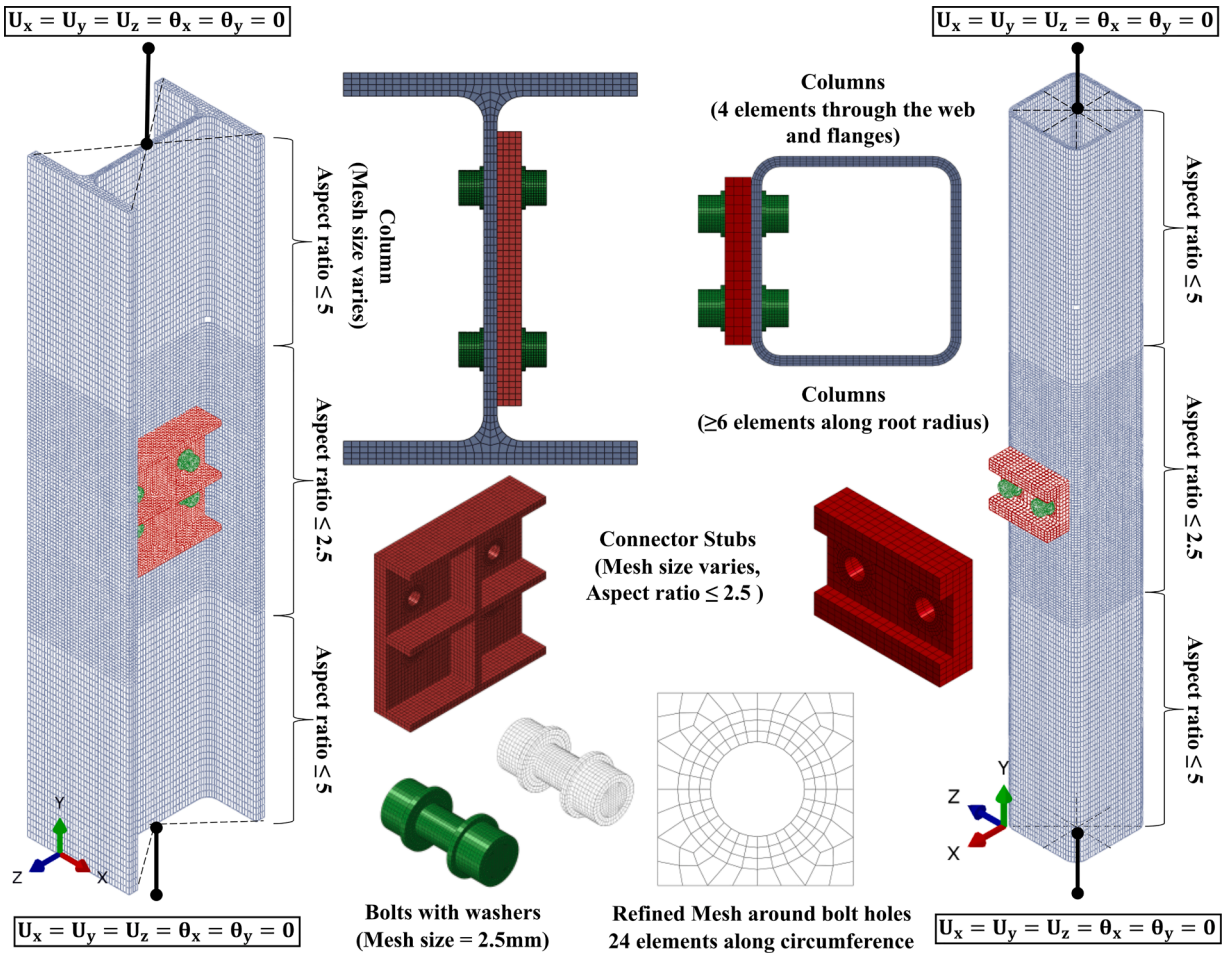

Fig. 18. FE models schematic details.

elements were found to be computationally expensive giving on average 4 times larger output database in size and lasting 6 times the time required to complete an analysis compared to the linear elements. For the C3D8R/I elements, on the other hand, the number of layers across the thickness affected the overall results significantly. Better accuracy of results closely matching those obtained from the quadratic elements was obtained when the thickness was partitioned into 3 or 4 layers. When using the reduced integration first-order brick element (C3D8R) enhanced section control was applied to suppress hourglass modes.

After performing an initial mesh sensitivity study, the numerical models were discretized using linear eight-node hexahedral elements with reduced integration (C3D8R) with four layers across the web thickness, which proved to be suitable for capturing bending behavior with reasonable accuracy. The static general solver was used and the first buckling mode corresponding to a single local bow-type imperfection of the web in the central zone was used to model local web initial geometrical imperfections with the amplitudes indicated in Table 3.

Three different parameters were monitored in the meshing process: the number of elements per thickness, the average aspect ratio of the elements, and the worst aspect ratios in the model. A Python script was written to systematically optimize the mesh size such that the average and worst aspect ratios do not exceed 2.5 and 5, respectively. Curvature control was imposed such that there would be about 8 elements per circular curve such as the root radius.

Given the different web thicknesses of the specimens, the mesh size varied from specimen to specimen and within the same model. In general, a finer mesh size of approximately 2 mm was used in the vicinity of the bolt holes, with 24 elements arranged around the circumference. The mesh size was coarser away from the loaded zone while maintaining an average element aspect ratio below 2.5. The bolts were modeled as a single part, and the washers were explicitly included in the models. The mesh size for the bolts was fine (2.5 mm), whereas the connector pieces were modeled with a coarser mesh, except in the region surrounding the bolt holes. Fig. 18 provides a schematic presentation of the model assembly, boundary conditions, and mesh details for specimens 2 and 5, for reference.

4.1.4. Loading

The load in the numerical models was introduced in the form of imposed displacements, similar to the tests that were displacement-controlled. To apply these displacements, the faces of the loading stubs were tied to a reference point located at the center of the tied geometry. The displacement load was applied to this reference point.

4.2. Model validation

The Finite Element Models (FEM) were validated against the test results comparing the following three aspects: the load-displacement curves, the deformations, and the stress/strain distribution in the web plates.

4.2.1. Force-displacement behavior

The relationship between the applied out-of-plane load and the web's net deformation as obtained from the tests and the calibrated numerical models is plotted in Fig. 19, highlighting the accuracy of the calibrated finite element models in terms of global behavior.

Good agreement can be seen for specimens 1, 3, and 4 during all phases of the specimens' responses. In the case of specimen 2, a good

match is seen at the elastic range and the bending knee of the curve with apparent deviations at the post-limit portion of the curve. The boundary condition change in the later stages of the test, as explained in previous sections, and the material difference between the web and flanges, which were yielding significantly, are assumed to be the reason for this difference. The test and FEA results demonstrate a reasonable agreement for the tubular column in specimen 5 during the initial stage. Both curves exhibit similar initial and post-yield stiffnesses. However, the numerical model tends to overestimate the bending resistance. This discrepancy may be attributed to challenges in accurately estimating the cross-sectional imperfections of the tube. Furthermore, the loading eccentricity could also contribute to this behavior.

At the onset of the loading stage, the material operates within an elastic state, characterized by small stresses well below the proportional limit, and material nonlinearity is not yet engaged. Simultaneously, the applied displacement is of such magnitude that the impacts of geometric non-linearities are virtually negligible. Consequently, during the initial stage, both linear and nonlinear analyses yield essentially identical results, except in cases featuring unusually high initial imperfections. The gap between linear and nonlinear analyses becomes more pronounced as the load/displacement is progressively increased. With higher deformations, there is an associated increase in strains and second-order effects. As the material undergoes yielding, relatively higher deformations manifest for the same load increment. The slope of the material's stress-strain curve gradually diminishes, paralleled by a decline in the force-displacement curve. In general, material nonlinearity tends to decrease stiffness, while geometric nonlinearity, aided by the contribution of membrane actions, tends to augment stiffness. The test results (Fig. 19) and subsequent numerical analyses (Fig. 30) confirm this assertion.

Curve fitting methodologies were used to calculate the initial, post-yield, and membrane stiffnesses. These calculations were based on the experimental results within specific regions on the curves, as indicated by the magenta, green, and black lines. The selection of regions of interest was supported by numerical derivations conducted on the force-displacement curve, allowing for the identification of critical inflection points. In the legend, the equation of the fitted straight lines is shown between parentheses, whereby the first number is the slope, while the second number represents the ordinate at the origin.

4.2.2. Deformations comparisons with DIC

The deformation profiles of the web plate along a vertical path at the center of the profiles are shown in Fig. 20. These deformations correspond to load levels close to the maxima observed during the tests, i.e., 571 kN, 810 kN, 998 kN, and 398 kN for the four specimens, respectively. A reasonable match is observed between the web deformation profiles obtained from the test (DIC) and the numerical simulation. The figure highlights the localized nature of the deformations along the length of the first three specimens through their bolt group centers. As was the case in the load-displacement behavior, deformations of the web in the fourth specimen – the girder – are also different from the preceding three specimens. Given the larger web depth and short total height of this specimen, the deformation is smoothly distributed vertically with no signs of localized deformations. Indeed, the web of this high-strength steel specimen was in the elastic range for the most part when the test was concluded due to the failure of a rod supporting the bottom hinge.

The DIC readings for the last specimen which is a tubular column were made at the back face of the section as physical constraints did not permit tracking the deformations of the loaded face. Therefore, a comparison like the foregoing cases is not made.

4.2.3. Stress and strain distributions

An important observation from the numerical results is the visualization of the stress and strain distribution internally within the specimens. It helps identify which parts sustained the most load and how much of the stretch around the loaded region went to the plastic range. Fig. 21 displays the stress distribution for each specimen at its maximum

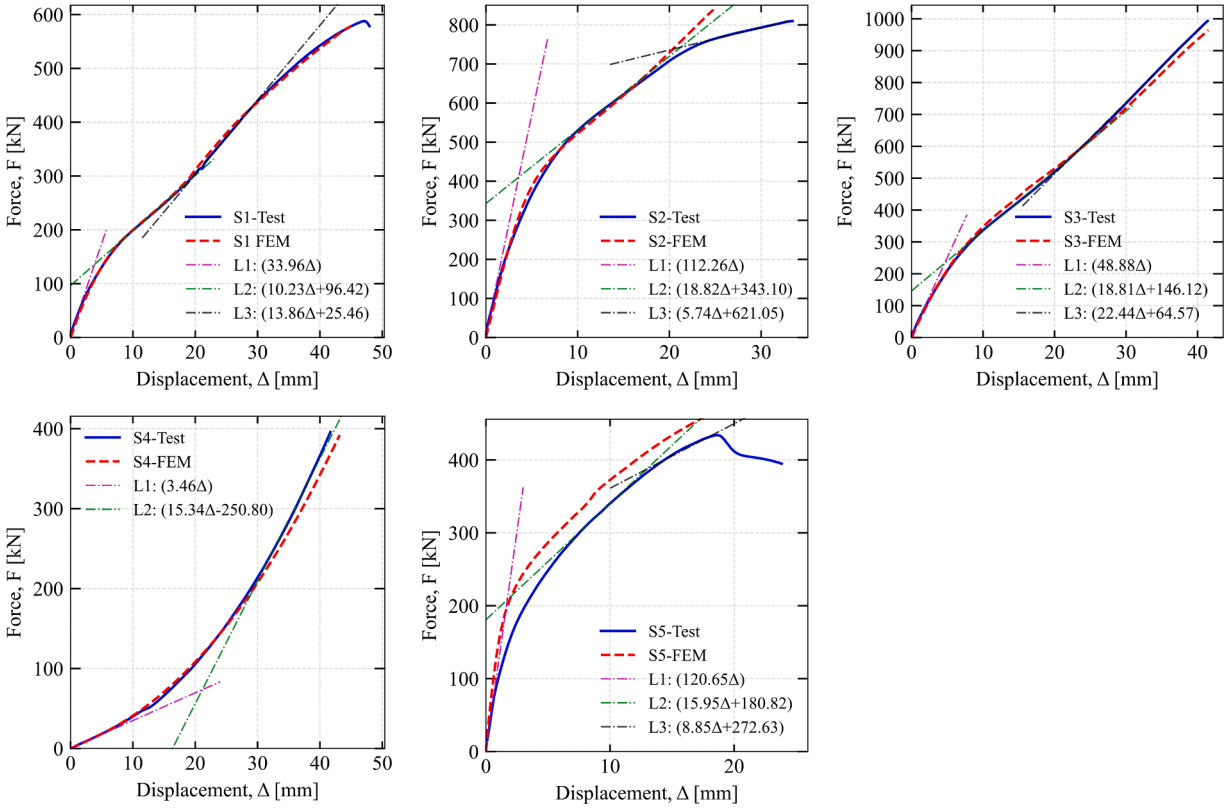

Fig. 19. Comparison between experimental and numerical results and evaluation of stiffness estimates from the tests.

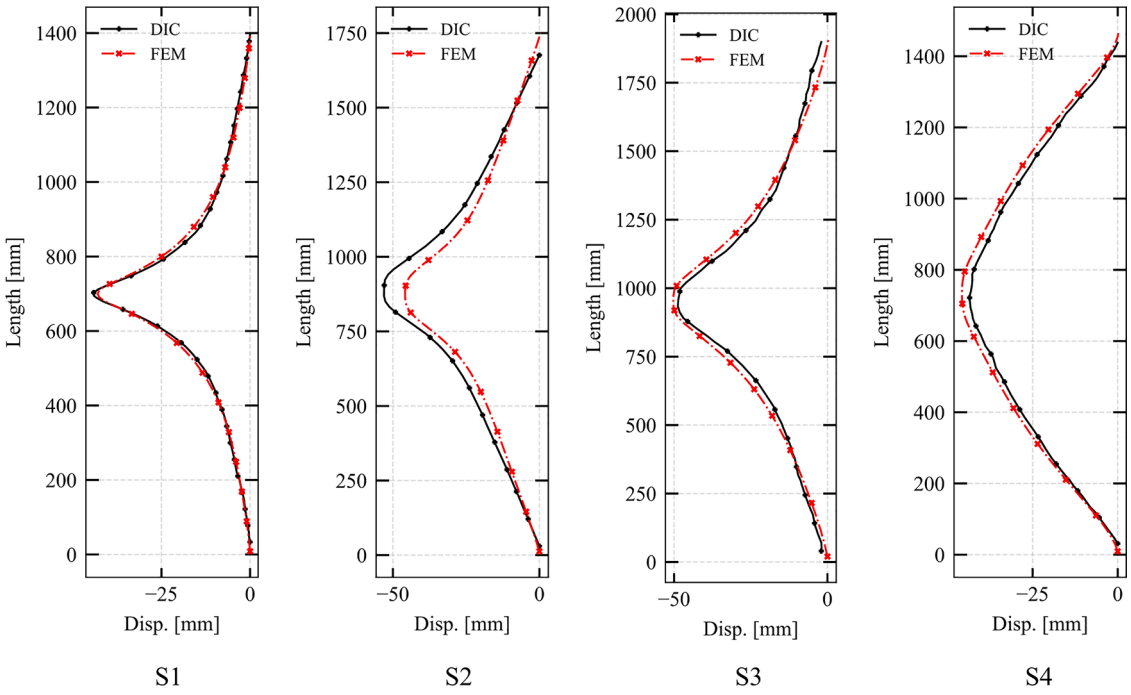

Fig. 20. Deformation profiles from DIC and calibrated FE models.

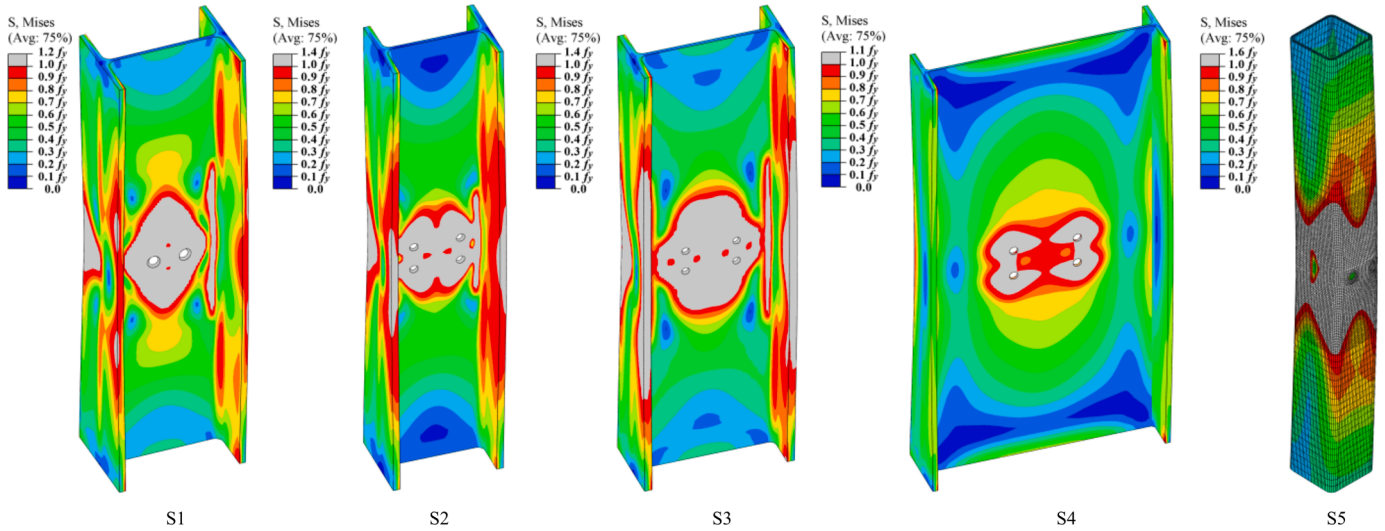

Fig. 21. Stress distribution at the maximum displacement load in the tests.

displacement load as observed from the tests.

It is evident at this stage of loading that in addition to the yielding of the column webs, plastification of the supporting flanges is actively ensuing. Larger yielded areas of the flanges on the tips that buckled inward are notable. However, the flange tips on the opening side also sustained yielding as was observed from the tests. Stresses that exceed the parent material yield stress have been color-mapped as gray for easy identification in Fig. 21.

The localization of high strains around the bolt holes is better exposed in the equivalent plastic strain (PEEQ) plots as shown in Fig. 22. Here PEEQ values above 0.1 % are selectively displayed for visual clarity. One can note from the plots that the highest strains are located on the outer half of the bolt holes where the web kinks consonant to the applied deformation.

The diagonal/radial yield cracks explained in the test results are a result of this strain distribution. Moreover, the bending and ultimate fracture of the washers starts from this zone where the stress concentration is high.

Fig. 23 shows the load-displacement plots with an accompanying plot showing the maximum equivalent plastic strain (PEEQ) at each step of analysis both in the vicinity of the bolt holes and the root radius edges for the first three specimens. The 5 % and 15 % PEEQ states have been chosen as round numbers to highlight two stages in the F-D plots. The 5 % PEEQ was chosen because it has recently been suggested as a limiting plastic strain in prEN 1993–1–14 [34]. The experimental results show that it is reached mostly after the bending 'knee' of the curve where yielding has occurred, but where membrane actions are still relatively low. The 15 % PEEQ is reached mainly around the bolt hole, at a stage where membrane actions are already high for the shown specimens.

The green and red lines on the right-hand side depict cuts at

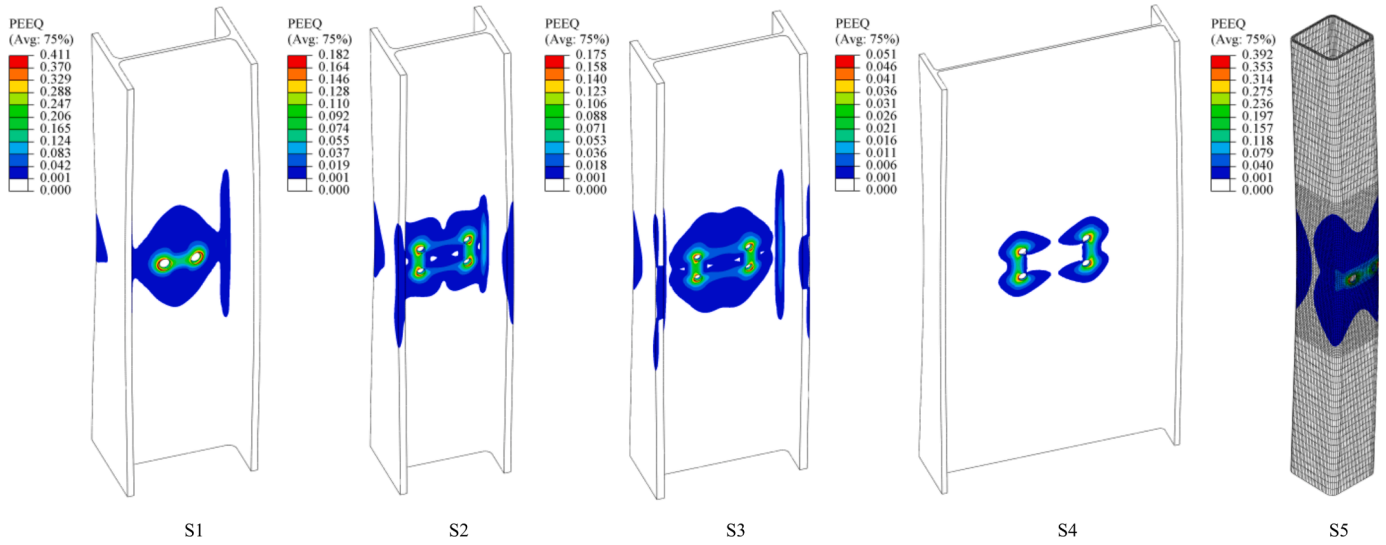

Fig. 22. PEEQ distribution at the maximum displacement load in the tests.

increments of 5 % and 15 % maximum plastic strains, marked by corresponding dots of the same color on the force-displacement plot (left-hand side). The solid and broken lines illustrate the strain profile on the front (outer) and back (inner) faces of the web, respectively. Notice how the specimens continue to resist additional load even at high PEEQ values. This is attributable to the fact that the strains are highly localized. To highlight this fact, three cuts showing the plastic strain profiles (i) vertically along the bolt columns, (ii) vertically along the edges, and (iii) horizontally along the bolt row centers are shown for the 5 % and 15 % maximum PEEQ increments. It can be noticed from these cuts that the strains on the back face are significantly lower than those from the outer face. Also, note how these strains drop by more than half at a bolt radius distance from the holes.

The observation made in the test that the washers sustain indentations and damage under higher loads is evident from the FEA results (Fig. 24). Once the web has deformed, the pressure distribution on the washers is no longer uniform. As a result, the washer edges closer to the flanges suffer the most damage and punching initiates from those sides. Punching resistance formulations based on load projection onto a flat surface (the undeformed shape) therefore can lead to unconservative estimates. In the two bolt row cases with more bolts carrying the load, the washers experience similar concentrated stresses, however, the indentations noted were lighter.

5. Parametric study

5.1. Definition

Based on the calibrated numerical models, a parametric study is devised to further explore the face plate behavior in open section minor axis connections. The definition of the parametric study is mostly based on the influence of the non-dimensional parameters shown in Fig. 25.

$$\alpha = \frac{c}{b_{clear}} \qquad \beta = \frac{\mathrm{d}}{\mathrm{b_{clear}}}$$
$$\mu = \frac{b_{clear}}{t} \qquad \zeta = \frac{\mathrm{d_{washer}}}{\mathrm{b_{clear}}} \tag{8}$$

where c is the vertical distance between washer edges $(W+d_{washer})$, d is the horizontal distance between washer edges on the same bolt row $(P+d_{washer})$, b_{clear} is the clear web depth, and t is the thickness of the web/face.

167 models are developed featuring 17 different column sections with web slenderness μ ranging from 14 to 80. While the sections with a web slenderness ratio between 14 and 46 were picked from commercial catalogs, those with 60, 70, and 80 were proposed as welded columns. The sections were strategically selected to enable the comparison of two sections of similar web slenderness but with different flange rotational support stiffness. Single and double bolt rows of connections with variable bolt spacings as shown in Table 4 were considered. The ratios of the horizontal bolt gage and vertical row pitch center-to-center distances to the web width were systematically chosen to range from 0.1 to 0.8 while maintaining practical spacings for each section. The specimen length was set to 6 times the web depth for all cases except for those with web depths higher than 500 mm where 4 times this depth was used as the specimen length. S355 steel has been used throughout the cases with the nominal properties defined. The material constitutive model presented in Fig. 26 was used according to the model described in [35].

5.2. Analysis of results

5.2.1. Global behavior

Fig. 27(a & b) illustrates the force-displacement curves for all cases, highlighting the positive correlation between web slenderness and resistance and stiffness. The role of boundary conditions on the face plate's behavior is shown in Fig. 28(a), that compares pairs of profiles, sharing equal web slenderness but differing in supporting flange stiffness and web thickness, exhibiting markedly distinct responses. For exemplification, the HEM400 profile and HEC320 profile, both possessing a web slenderness ratio of 14, demonstrate different stiffness and resistance. The flanges of the first profile provide 2.24 times stiffer supports compared to the latter. At the same time, the latter possess 1.31 times thicker web plate. Lastly, an increase in bolt spacing, i.e., closer proximity of the bolt holes to the supports, correlates with elevated stiffness and resistance, as well as reduced ductility, as illustrated in Fig. 28(b).

In Fig. 28, the annotations placed on the curves denote points at which a maximum plastic strain (PEEQ) value reaches 5 % (represented by a circle), 10 % (represented by a rectangle), and 15 % (represented by a Tri-down symbol). The solid or closed symbols denote instances when this threshold is reached anywhere in the web, while the corresponding

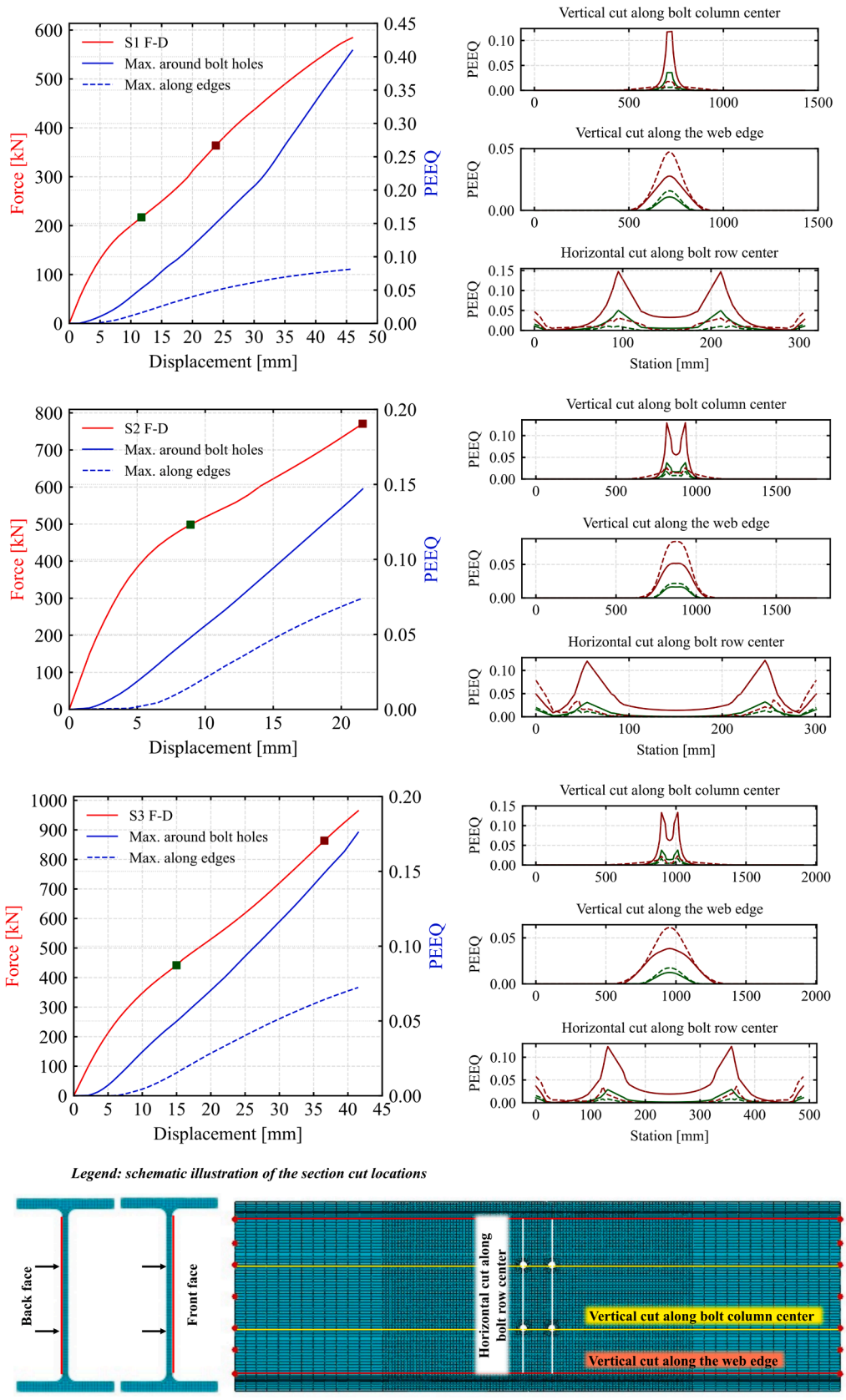

Legend: schematic illustration of the section cut locations

Fig. 23. Maximum PEEQ progression and strain profiles at critical locations.

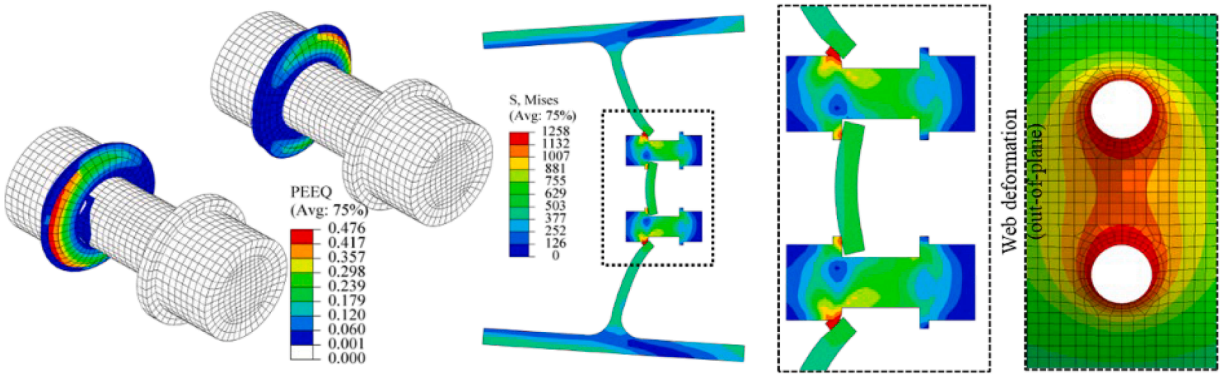

Fig. 24. Bolt hole, washer, and web deformations.

open shapes signify occasions when the mean PEEQ reaches the specified value in the web area surrounding the bolt holes, bound by one-third of the washer width. The observations indicate that the 5 % PEEQ is usually reached some increments after passing the bending knee on the load-displacement plot. It is important to note that the maximum plastic strain is in all cases observed around the bolt holes.

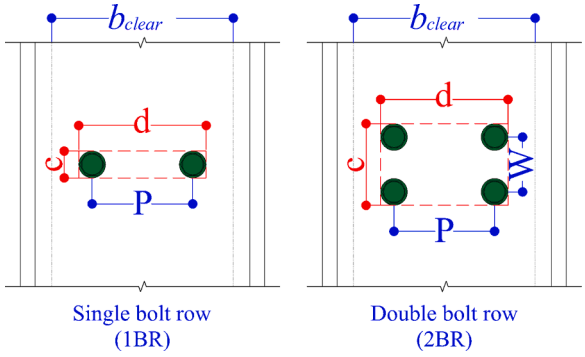

Fig. 25. Definition of geometric parameters.

The influence of bolt row spacing on the group effect in cases with two bolt rows is depicted in Fig. 29. For example, when comparing the single bolt row case to the largest double bolt row case considered (w = 185 mm), there was an observed increase of 79 % in resistance and 59 % in initial stiffness. This observation underscores that the response of the group is not twice that of the individual bolt rows, even in cases where the row spacings closely approach the clear web depth, particularly in connections where the column flanges are unrestrained. Tables A1,A2, A3 in the annex summarize the results of the parametric study.

5.2.2. *Influence of membrane effects*

The experimental results and the calibrated numerical simulations have clearly shown the large influence of membrane effects. To assess the membrane effects, first-order material nonlinear analyses (MNA) were additionally carried out for each test. Fig. 30 compares the force-displacement plots from MNA and GMNIA, showing the significant contribution of membrane forces, that varies from 12.9 % for Specimen 2 to 65.6 % for Specimen 4 at the maximum displacement load levels reached in the tests.

Table 4
Parametric study cases [units: mm].

Cases	Profile	d_w/t_w	Bolt	P (1BR) $W = 0$	Cases	[P,W] (2BR)	
01–06	HE 320 C	14	M24	P: [65;90;110;135;160;170]	**57–62**	Pairs 1	[65,65];[90,75];[110,85];[135,95];[160,105];[170,115]
					113–124	*Pairs 2*	*[65,85];[65,105];[65,125];[65,145];[65,165];[65,185];[110,65];[110,125];[110,185];[170,65];[170,125];[170,185]*
07–10	HE 400 M	14	M24	P: [90;120;150;180]	**63–66**	Pairs 1	[90,75];[120,85];[150,95];[180,105]
11–16	HE 320 B	20	M20	P: [65;90;110;135;160;170]	**67–72**	Pairs 1	[65,60];[90,70];[110,80];[135,90];[160,100];[170,110]
					125–132	*Pairs 2*	*[65,120];[65,180];[110,60];[110,120];[110,180];[170,60];[170,120];[170,180]*
17–18	HE 200 A	21	M20	P: [65;80]	**73–74**	Pairs 1	[65,60];[80,70]
19–22	HE 450 B	25	M20	P: [70;105;140;170]	**75–78**	Pairs 1	[70,60];[105,70];[140,80];[170,90]
					133–139	*Pairs 2*	*[70,100];[70,140];[70,180];[170,60];[170,100];[170,140];[170,180]*
23–28	HE 320 A	25	M20	P: [65;90;110;135;160]	**79–84**	Pairs 1	[65,60];[90,70];[110,80];[135,90];[160,100]
29–31	HE 550 B	29	M20	P: [90;130;175]	**85–87**	Pairs 1	[90,60];[130,90];[175,120]
					140–147	*Pairs 2*	*[90,120];[90,180];[130,60];[130,120];[130,180];[175,60];[175,120];[175,180]*
32–35	HE 450 A	30	M20	P: [70;100;135;170]	**88–91**	Pairs 1	[70,60];[100,70];[135,80];[170,90]
36–37	HE 700 B	34	M20	P: [115;175]	**92–93**	Pairs 1	[115,80];[175,100]
					148–152	*Pairs 2*	*[115,140];[115,200];[175,80];[175,140];[175,200]*
38–40	HE 550 A	35	M20	P: [85;130;175]	**94–96**	Pairs 1	[85,60];[130,70];[175,80]
41–42	HE 700 A	40	M20	P: [115;175]	**97–98**	Pairs 1	[115,60];[175,70]
					153–158	*Pairs 2*	*[115,80];[115,140];[115,200];[175,80];[175,140];[175,200]*
43–45	HE 600 AA	41	M20	P: [95;145;195]	**99–101**	Pairs 1	[95,60];[145,70];[195,80]
46–47	HE 800 A	45	M20	P: [65;135]	**102–103**	Pairs 1	[65,60];[135,70]
					159–163	*Pairs 2*	*[65,120];[65,180];[135,60];[135,120];[135,180]*
48–49	HE 1000 B	46	M20	P: [85;175]	**104–105**	Pairs 1	[85,70];[175,90]
50–53	HG 520 × 300	60	M20	P: [60;120;180]	**106–109**	Pairs 1	[60,60];[120,80];[180,100]
53–54	HG 600 × 300	70	M20	P: [70;140]	**109–110**	Pairs 1	[70,60];[140,80]
					163–167	*Pairs 2*	*[70,120];[70,180];[140,60];[140,120];[140,180]*
55–56	HG 680 × 300	80	M20	P: [80;160]	**111–112**	Pairs 1	[80,60];[160,80]

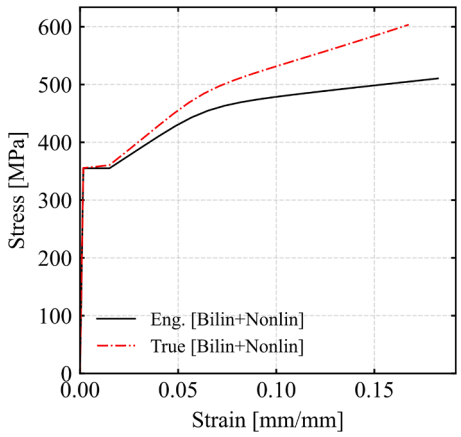

Fig. 26. Nominal S355 material model adopted for the parametric analysis.

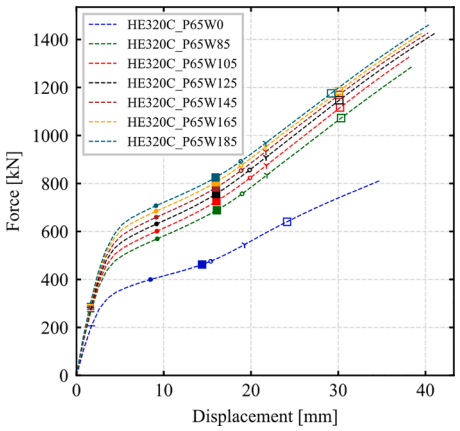

Fig. 29. Group effect comparing single and double bolt row cases.

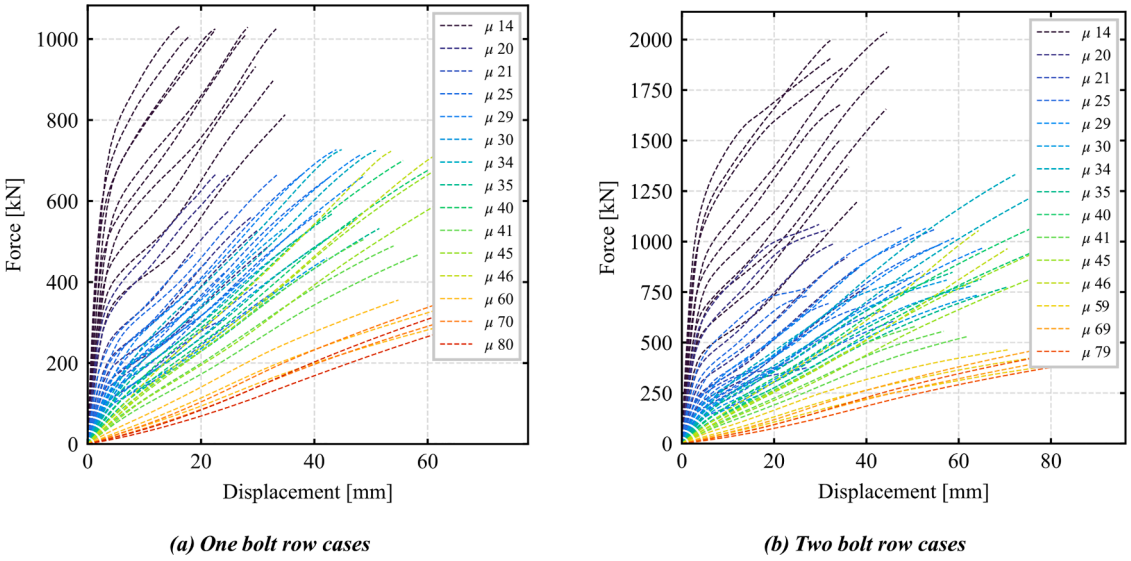

Fig. 27. Force displacement plots of all parametric study cases.

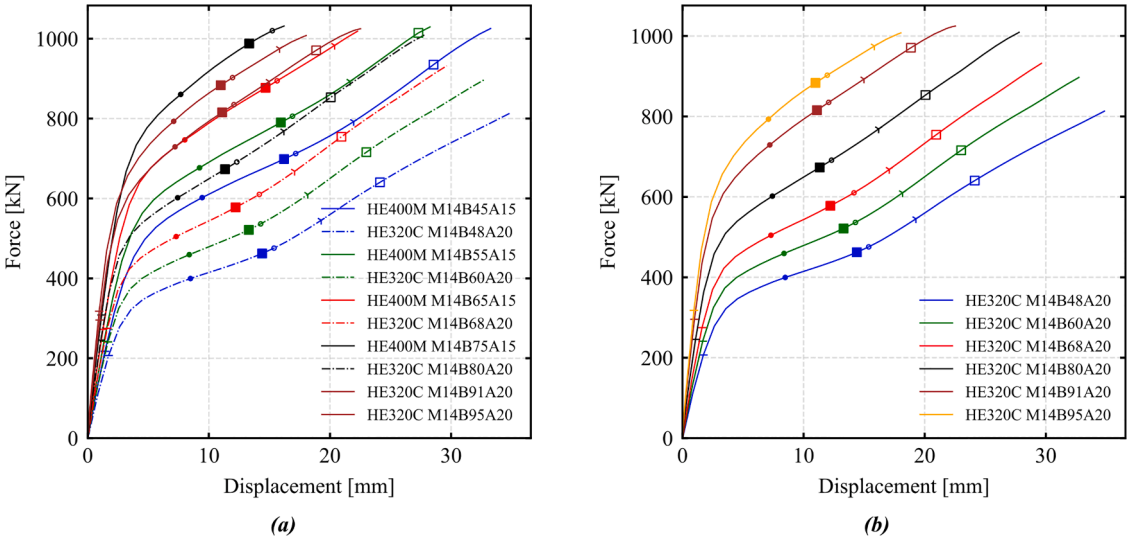

Fig. 28. Influence of (a) flange stiffness & web thickness and (b) bolt spacing.

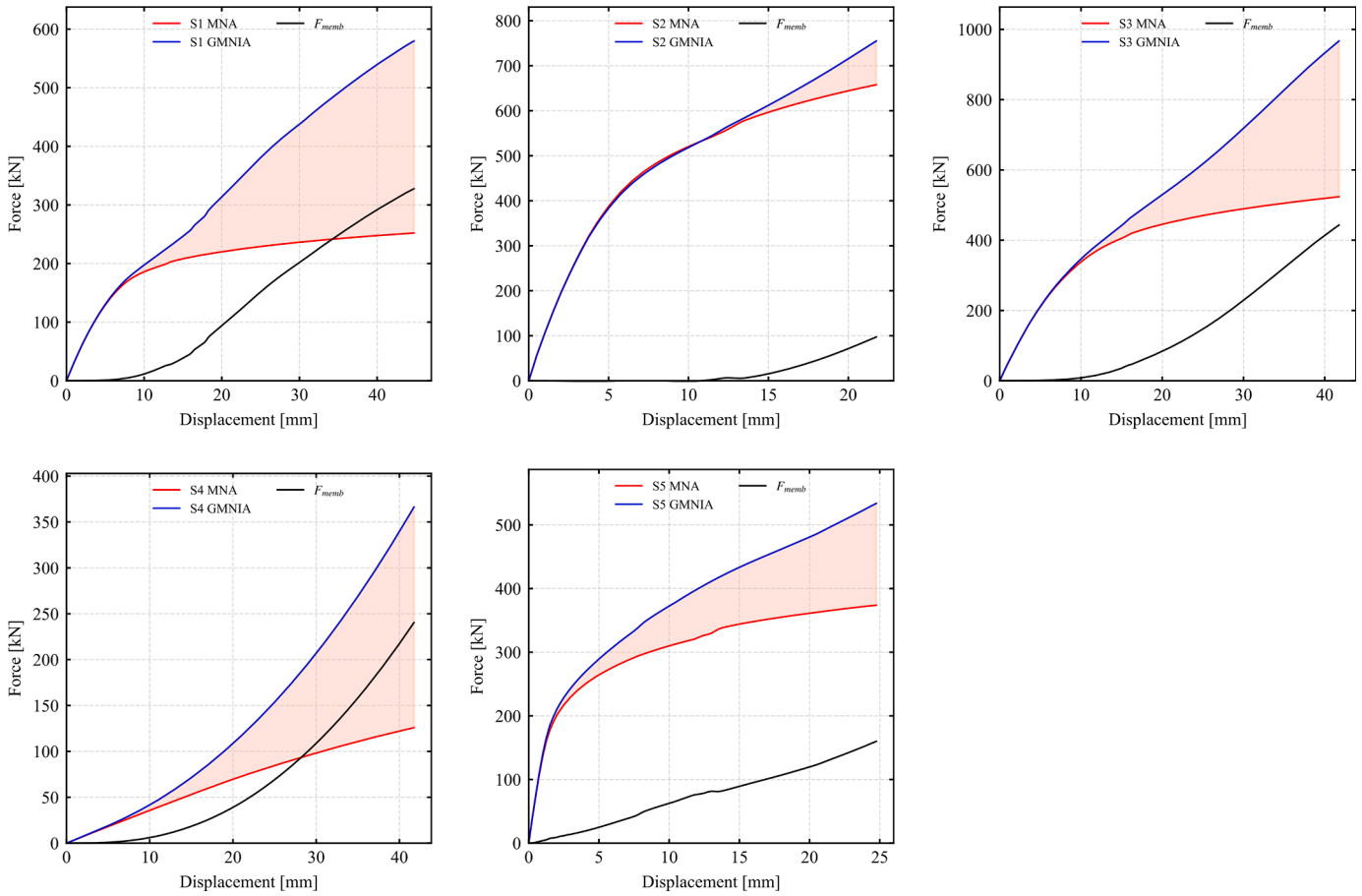

Fig. 30. Membrane force effects.

5.2.3. Influence of out-of-plane pushing force

The face plate component may be loaded out-of-plane by a pulling force (e.g. through the application of a pulling force transferred through bolts or a plate welded to the web of the column) or by a pushing force (e.g. a fin plate welded to the web or an endplate/beam flange in compression). In the literature, irrespective of the load introduction coming from bolts in tension, the contact of a plate, or a welded plate, the loaded area is invariably defined as an equivalent rectangular area. This was the case for the experimental tests described in this paper, all corresponding to out-of-plane loading by a pulling force transferred by pairs of bolts attached to the column web. The equivalent loaded area was defined according to Fig. 25, as a rectangle of width d (horizontal distance between washer edges on the same bolt row $(P+d_{washer})$) and height c (vertical distance between washer edges $(W+d_{washer})$). The

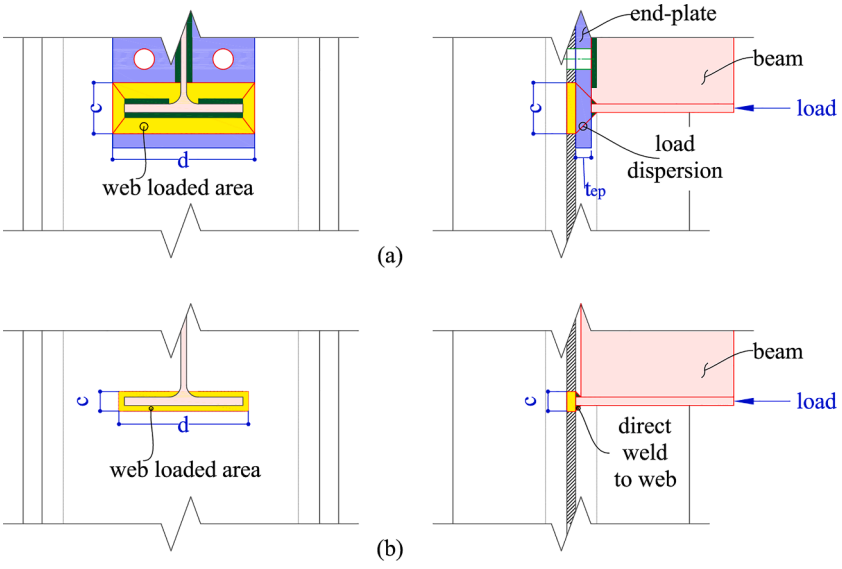

Fig. 31. Definition of an equivalent loaded area for a pushing force transferred through (a) endplate or (b) direct weld.

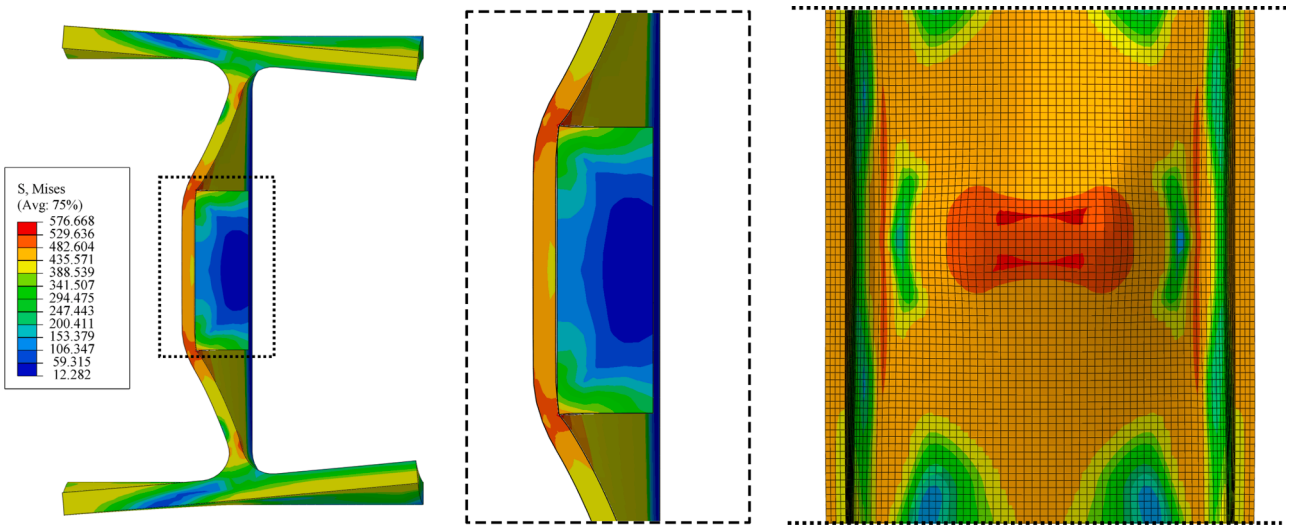

Fig. 32. Web deformations and stress distribution for a pushing force applied through contact.

equivalent loaded area for a pushing force transferred to the web through contact from a beam flange welded to an endplate is defined in Fig. 31a, while for pushing forces from flanges directly welded to the column web, it is defined in Fig. 31b.

In the case of the web of an I-section column, because of symmetry with respect to the mid-plane of the web, the two situations are identical. Small differences exist for the following reasons: (i) differences resulting from the size of the loaded areas: the assumption of an equivalent rectangular loaded area is not exact and varies between pulling (Fig. 24) and pushing (Fig. 32). (ii) differences resulting from the flexibility of the face plate between bolts that do not exist in the case of a pushing force (Fig. 32). This difference is contemplated in the theoretical model for the initial stiffness of the face plate [23] which considers flexible conditions at the bolt's axes and restrained conditions for stiff plates.

To clarify whether these differences are relevant, the five tested specimens were also modelled with a pushing load, using the same FE models described in Section 4.1 but with the following modifications: the bolts were replaced by a rigid plate that represented the vertical and horizontal distances between the washer edges of the bolt group.

Fig. 33 shows the differences between the numerical models for pulling and pushing forces for specimens S1 to S4. Hardly any effect is visible for the initial elastic stiffness because the membrane forces are negligible. However, for large displacements, the differences become relevant due to second-order effects.

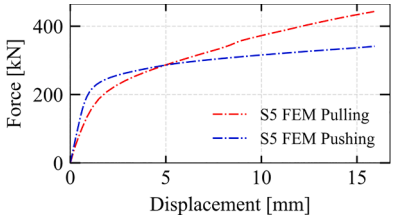

Fig. 34. Force-displacement curves for pulling and pushing forces (Tubular column).

In case of the face of a tubular column, the two situations are different because there is no symmetry with respect to the mid-plane of the face. In this case, a marked difference exists (Fig. 34) already for the initial stiffness because of the rounding transition between the faces of the RHS tube.

6. Assessment of analytical formulations for initial stiffness

This section compares the experimental/numerical results with selected theoretical models for initial stiffness available in the literature and proposes an improvement to the Conde et al. model that was

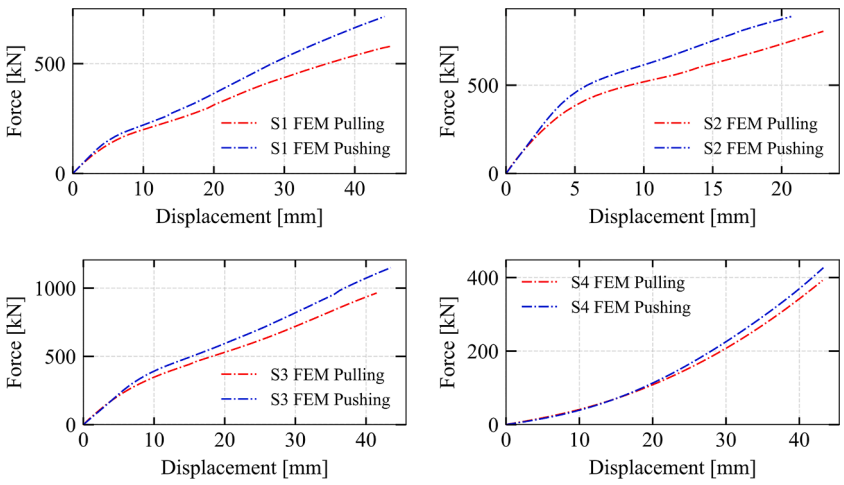

Fig. 33. Force-displacement curves for pulling and pushing forces (I-section columns).

recently developed by the authors.

6.1. Analytical models

The selected formulations are those proposed by Park et al. [20,21], Neves et al. [36], and Conde et al. [23]. Detailed explanations and further details regarding these formulations are described in [23]. Table 5 summarizes the corresponding application rules. where E is the Young's modulus, G is the shear modulus, ν is the Poisson's ratio, t is the web thickness, b is the face plate length, h is the tube depth for RHS, s is the supporting flange rotational stiffness, n is the distance from the face edge to the bolt center, d_m is defined as the mean of the across points and across flats dimensions of the bolt head or the nut, whichever is smaller, in cases where washers are absent. In instances where washers are utilized, d_m refers to the outer diameter of the washers.

All methods require the definition of the width of the face plate component because both open I-sections and RHS tubular sections present smooth circular transitions between the straight portion of the web/face and the flanges/side walls. The Neves model proposes the following expression:

$$b_{NEVES} = h_c - 2\left(t_{fc} + 0.5r_c\right) \tag{9}$$

while the Park and Wang model assumes that the 'deformable width' of the face is given as the clear width of the web:

$$b_{PARK} = h_c - 2\left(t_{fc} + r_c\right) \tag{10}$$

In case of the Conde et al. model, no specific recommendations regarding the estimation of this width were given [23]. Here, the net distance between the centerlines of the flanges is initially adopted, with the rationale that the support stiffness is computed at their centroidal axis.

$$b^{ref}_{CONDE} = h_c - t_{fc} \tag{11}$$

where h_c denotes the total depth of the column cross-section, t_{fc} is the flange thickness and r_c is the root radius of the flange to web. Concerning support rotational stiffness, Neves proposed applying a reduction factor to the initial stiffness calculated for the fully fixed flange case, as shown in Table 5. The formulation proposed by Park and Wang inherently incorporates the support stiffness using the expressions below.

$$s = \frac{2Et^3_{fc}}{12b_f} \quad : \text{for I/H profile flanges} \tag{12}$$

$$s = \frac{4Et^3_{fc}}{12h_c}\left(\frac{h_c + 1.5b_c}{h_c + 2b_c}\right) \quad : \text{for RHS chords} \tag{13}$$

Finally, for the Conde et al. model, in the absence of specific guidance in [23], the rotational stiffness provided by the flanges and side walls per unit length is considered according to Eqs. (12) and (13).

Table 5
Initial stiffness according to Park [20], Neves [36] and Conde [23].

Park	$K_{ini.PARK} = E\dfrac{f_1\, t^3}{b^2 m \cos\left(\frac{n\pi}{2b}\right)}$
	$f_1 = \dfrac{11.5\, b\, k_r + 5.7\, E\, t^3 \times 1mm.}{2.024\, b\, k_r\, m - b\, k_r + E\, m\, t^3 \times 1mm.}$
	$k_r = \begin{cases} \dfrac{2EI}{h} & : \text{I} - \text{section} \\ \dfrac{4EI}{h}\left(\dfrac{1.5b+h}{2.0b+h}\right) & : \text{RHS} \end{cases}$
	$m = 0.143\left(\dfrac{n}{b}\right)^2 - 0.306\left(\dfrac{n}{b}\right) + 1.076$
Neves	$K_{ini.fixedflanges} = 16\dfrac{E\, t^3}{b^2}\dfrac{\alpha + (1-\beta)\tan\theta}{(1-\beta)^3 + 10.4(k_1 - k_2\beta)/\mu^2}$
where	$k_1 = 1.5$ and $k_2 = 1.6$
	$K_{ini.freeflanges} = f_{reduction} K_{ini.fixedflanges}$
	$f_{reduction} = \min\left(\dfrac{(\mu/\beta)^{1.25}}{230}, 1\right)$
	$\theta = \begin{cases} 35 - 10\beta, & \beta < 0.7 \\ 49 - 30\beta, & \beta \geq 0.7 \end{cases}$
	Valid for: $\begin{Bmatrix} 10 \leq \mu \leq 50 \\ 0.08 \leq \beta \leq 0.75 \\ 0.05 \leq \alpha \leq 0.2 \end{Bmatrix}$
Conde	$K_{ini.CONDE} = r\left(8EI_1\lambda^3 + k_3\, c\right)$
	where : $r = 2, \quad e = b/2 \quad c = w + d_m, \quad \lambda = \sqrt[4]{\dfrac{k_2}{4EI_1}}$
	$EI_2 = \dfrac{Et^3}{12(1-\nu^2)}, \quad EI_1 = eEI_2, \quad GA_v = \dfrac{2Gt}{3}$
	$d_3 = \dfrac{n^3 s(2b-3n) + 2EI_2 n^2(4n-3b)}{6EI_2(2EI_2 + bs)} + \dfrac{n}{GA_v}$
	$d_2 = \dfrac{n^3}{12EI_2}\dfrac{sn + 4EI_2}{sn + EI_2} + \dfrac{n}{GA_v}$; $k_2 = \dfrac{1}{d_2}$ and $k_3 = \dfrac{1}{d_3}$

6.2. Comparison with test results

Table 6 and Fig. 35 compare the three formulations against the test results. In Fig. 35, the shaded (hatched) regions delineate the anticipated range between the lower edge, representing results for pinned supports, and the upper line, depicting the expected stiffness ratio when full restraint is provided by the flanges. The model proposed by Park and Wang overestimates the initial stiffness (average 157 %). Likewise, the Neves et al. model leads to a strong overestimation of the initial stiffness (average 182 %).

Using Eq. (11) for the plate length, the Conde et al. model produces accurate results in comparison to all test outcomes, with an average of 88 % and a coefficient of variation of 13 % and a maximum deviation of approximately 24 % for test S5 (tubular column specimen).

6.3. Comparison with parametric study results

6.3.1. Single bolt row cases

Fig. 36 presents a comparison of the initial stiffness estimates obtained using the analytical models summarized in Section 6.1 with the numerical results of the parametric study. The Neves' formulation tends to overestimate the initial stiffness significantly; even disregarding the high peaks observed in cases where the β values exceed the range of validity for the expressions a maximum difference of 250 % is reached for cases characterized by higher web slenderness ratios (>25). For lower web slenderness ratios, the estimates generally lean towards the conservative side, albeit without a consistent trend.

Similarly, the formulation by Park and Wang appears to overestimate the initial stiffness across all ranges on average. The proposal by Conde et al. predominantly yields conservative estimates, particularly as the bolt spacing increases for web slenderness ratios below 30. Some overestimation is noticeable beyond this web slenderness ratio, especially for smaller pitch distances where the load is concentrated at mid-span. A common trend observed for the last two formulations is that the stiffness ratios decrease as the bolt spacing is increased (increasing β). This trend will be further discussed in Section 6.4.

6.3.2. Double bolt row cases

Fig. 37 compares similar results for double bolt row cases. The same observations provided for the single bolt row cases are valid here too. Neves' formulation significantly overestimates initial stiffness, reaching 300 % for higher web slenderness ratios (>25). Park's formulation generally overestimates across all ranges, while Conde et al.'s tends to be conservative with increased bolt spacing for web slenderness ratios

Table 6
Initial stiffness estimates – Test & Analytical methods [units: kN/mm].

Sp.	Test	Park et al		Neves et al		Conde et al		
		Semi-rigid	Pinned	Fixed	Semi-rigid	Pinned	Fixed	Semi-rigid
S1	34.0	38.8	21.8	87.1	87.1	11.6	37.5	27.2
S2	112.3	228.8	79.5	317.9	131.4	34.0	142.9	95.1
S3	48.9	83.4	35.1	140.4	140.4	14.9	55.1	44.5
S4	3.5	5.6	1.7	6.9	6.9	1.2	4.2	3.8
S5	120.7	167.4	55.8	223.4	62.2	53.4	220.7	91.5
Avg*		157%	60%	242%	182%	35%	131%	88%
COV**		19%	18%	18%	48%	15%	21%	13%

* Averages of the initial stiffnesses obtained analytically in comparison to the test results.
** Coefficient of variation of the analytical estimates with respect to those obtained from the tests.

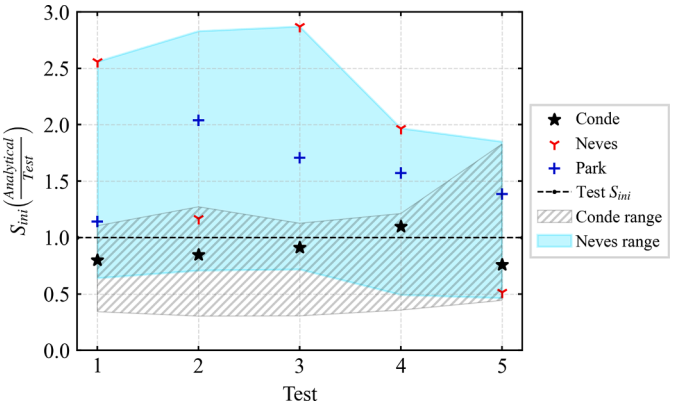

Fig. 35. A comparison of initial stiffness: Test vs analytical formulations.

below 30. Stiffness ratios decrease with increased bolt spacing for the latter two formulations (increasing β). This trend will be further discussed in Section 6.4.

Notably, the formulation by Park is developed to estimate stiffness row-by-row and the vertical spacing between rows is not considered in the formulation. The authors indicated in [20] that consecutive bolt rows would be considered to act as parallel individual components/springs working together in essence leading to twice the individual stiffness for a double bolt-row connection under direct tension. As a result, it completely disregards interaction between bolt rows. From the parametric analyses in this paper, it has been shown in Fig. 29 that the group stiffness and resistance are not equal to the summation of the individual row resistance and stiffness for most practical bolt row spacings.

6.3.3. Summary

Table 7 provides a comparative analysis of numerical results with three analytical models outlined in Section 6.1. The comparison is presented as the ratio of analytical estimates to numerical results. While detailed results are available in the annex, here they are grouped and averaged for each web slenderness range for clarity. The average initial stiffness obtained through the Conde formulation, categorized by web slenderness, varied from 0.73 to 1.35 times those obtained from FEA. Estimates from Park's and Neves' formulations ranged from 0.61 to 1.57 and 0.38 to 2.46, respectively, indicating higher variability. In the case of double bolt row connections, Conde's formulation produced fairly accurate results with ratios between 0.62 and 1.38. Neves' formulation displayed notable variability (0.57–2.75), while Park's formulation produced higher estimates (1.09–2.48) compared to FEA, primarily due to its oversight of the group effect, resulting from a doubling of the single-row stiffness computation. The root mean square error (RMSE) between the initial stiffness observed in the numerical analysis and the predictions from the three formulations distinctly establishes the advantage of Conde's model. Across all cases studied, the RMSE for Park's, Neves', and Conde's models stand at 91.1 %, 110 %, and 25.2 %, respectively.

6.4. Improvement of the Conde et al. [23] method: calibration of the length of the face plate

Several shortcomings can be identified in the formulations, including: (i) the empirical definition of the width of the equivalent beam strip in Neves' model, (ii) disregarding group effects for more than one bolt rows in Park and Wang's method, (iii) the assumption of a constant length of the face plate, despite evident variations in support rotational stiffnesses for connections to columns with unrestrained flanges in both Park's & Neves' methods, and (iv) the inadequate representation of bending deformation patterns, particularly for higher bolt

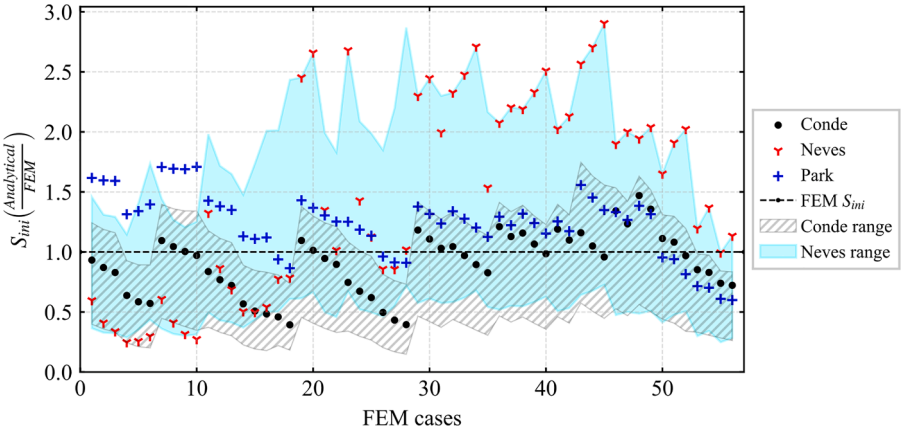

Fig. 36. A comparison of initial stiffness: 1BR Parametric FEA vs analytical formulations.

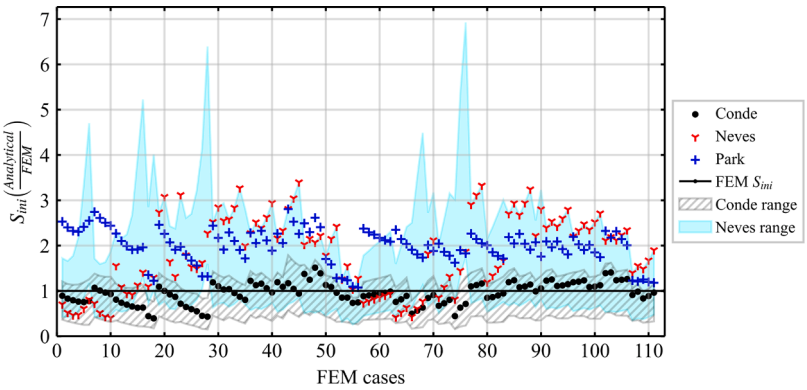

Fig. 37. A comparison of initial stiffness: 2BR Parametric FEA vs analytical formulations.

Table 7
Initial stiffness estimates statistics – Parametric study & Analytical methods.

Case Group	S_{ini} Park/S_{ini} FEM			S_{ini} Neves/S_{ini} FEM			S_{ini} Conde/S_{ini} FEM		
	Avg [-]	COV [%]	RMSE [%]	Avg [-]	COV [%]	RMSE [%]	Avg [-]	COV [%]	RMSE [%]
1BR M14	1.57	9.5	58.5	0.38	33.4	63.7	0.85	21.5	23.4
1BR M20	1.16	16.5	25.3	0.75	34.0	35.8	0.59	25.6	43.5
1BR M25	1.17	15.2	24.7	1.54	46.2	89.8	0.73	32.4	35.8
1BR M30	1.27	6.3	28.0	2.26	15.7	130.4	1.01	11.2	11.3
1BR M35	1.25	4.6	25.3	2.26	6.6	127.1	1.11	7.0	13.5
1BR M40	1.36	10.1	38.2	2.46	13.7	150.3	1.09	7.5	12.2
1BR M45	1.33	3.3	32.9	1.97	2.6	97.5	1.35	6.3	36.3
1BR M60	0.90	6.4	11.5	1.86	8.7	87.4	1.05	5.4	7.7
1BR M70	0.71	0.7	29.5	1.28	7.0	29.1	0.84	1.1	16.3
1BR M80	0.61	0.2	39.5	1.07	7.2	10.1	0.73	0.5	26.8
1BR Total	**1.24**	**21.6**	**35.6**	**1.48**	**55.7**	**95.2**	**0.9**	**28.9**	**27.8**
2BR P1 M14	2.48	5.1	148.8	0.57	23.2	45.4	0.88	12.1	16.2
2BR P1 M20	1.84	18.4	90.7	1.18	17.8	27.5	0.62	21.1	39.8
2BR P1 M25	1.83	19.6	90.7	2.06	31.7	124.4	0.73	30.3	35.1
2BR P1 M30	2.08	11.1	110.2	2.66	13.7	169.8	1.00	12.3	12.3
2BR P1 M35	2.13	7.5	114.4	2.55	9.0	156.6	1.11	8.0	13.8
2BR P1 M40	2.38	10.8	140.8	2.75	16.4	180.8	1.09	8.4	12.6
2BR P1 M45	2.46	4.8	146.0	2.12	3.5	112.0	1.38	6.9	39.3
2BR P1 M60	1.52	11.6	54.7	2.11	12.3	113.8	1.05	6.9	9.1
2BR P1 M70	1.26	1.8	25.9	1.41	10.3	43.4	0.85	0.1	14.5
2BR P1 M80	1.09	1.4	8.9	1.16	9.9	19.5	0.74	0.1	25.7
2BR P2 M14	2.14	10.3	115.9	0.70	23.3	34.1	0.82	18.6	23.7
2BR P2 M20	1.91	9.0	92.6	1.43	30.3	61.0	0.73	17.8	30.2
2BR P2 M25	2.03	11.6	105.9	2.22	37.0	147.2	1.00	12.0	12.1
2BR P2 M30	2.07	9.3	108.8	2.73	10.2	175.5	1.11	7.0	13.7
2BR P2 M35	2.03	7.4	103.8	2.51	6.6	151.5	1.18	4.7	18.8
2BR P2 M40	1.95	7.3	96.4	2.43	6.7	144.0	1.16	4.9	16.5
2BR P2 M45	2.24	6.9	125.3	2.17	4.8	117.6	1.32	5.5	32.8
2BR P2 M70	1.22	2.9	22.8	1.55	13.2	58.4	0.91	5.6	10.7
2BR Total	**2.01**	**19.3**	**107.7**	**1.82**	**45.6**	**116.9**	**0.95**	**24.6**	**23.9**
Total	**1.76**	**28.6**	**91.1**	**1.71**	**49.3**	**110.4**	**0.94**	**26.1**	**25.2**

• P1 and P2 indicate Pairs 1 and 2 respectively.

spacings in all the three methods, among others.

The Conde et al. model was developed assuming that an appropriate length of the face plate was available as input. Hence, it is necessary to provide guidance for the choice of the length of the face plate. Taking advantage of the experimental evidence and the results of the parametric study, Fig. 38 illustrates the variation of the initial stiffness ratios using the Conde's formulation with the non-dimensional ratios ζ, β, and μ. A good correlation is identified with a quadratic correction coefficient that depends on the product $\zeta\beta\mu$.

Hence, an effective length of the face plate was calibrated with the reference length of Eq. (11),

$b^{ref}_{CONDE} = h_c - t_{fc}$, using a quadratic correction factor (ψ) that depends on the product $\zeta\beta\mu$. Fig. 39 illustrates the application of this correction factor, defined in Eq. (14) as follows:

$$b^{eff}_{CONDE} = \psi \cdot b^{ref}_{CONDE}, \quad \text{where } \psi = 0.0198(\zeta\beta\mu)^2 - 0.1806(\zeta\beta\mu) + 1.1893 \tag{14}$$

Fig. 40 and Table 8 show a comparative analysis of the results of the parametric study versus the Conde et al. model both using b^{ref}_{CONDE} and b^{eff}_{CONDE}, showcasing enhanced estimates with reduced scatter and increased consistency.

The range between the minimum and maximum ratios of analytical to numerical stiffness for each group has been narrowed, with the average closely approaching 1. This improvement is particularly evident in commercial profiles with a web slenderness less than 60.

With the proposed enhancement, deviations higher than 20 % from the parametric analysis were observed in only about 10.8 % of cases, primarily in double bolt row cases, where the product $\alpha\beta\mu$ is larger than 8. Characteristic cases include connections to stocky columns with β

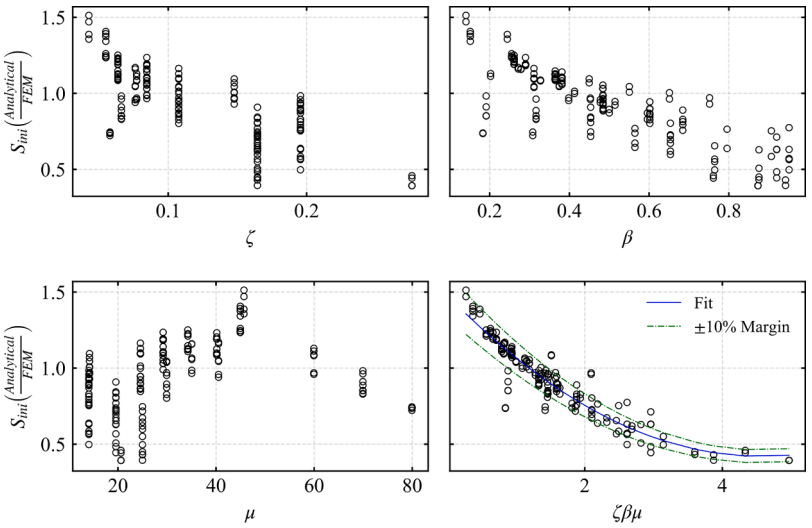

Fig. 38. Correlation of the initial stiffness ratios using the Conde's formulation with the non-dimensional ratios ζ, β, and μ.

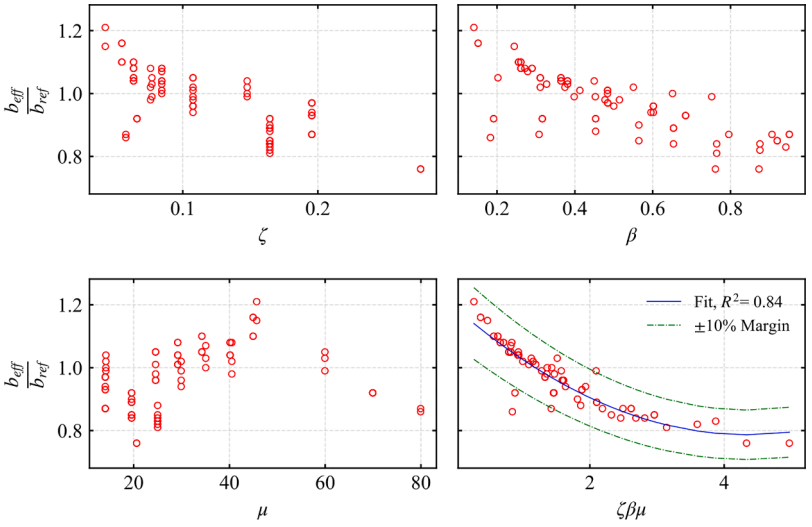

Fig. 39. Calibration of the effective length in the Conde et al. model.

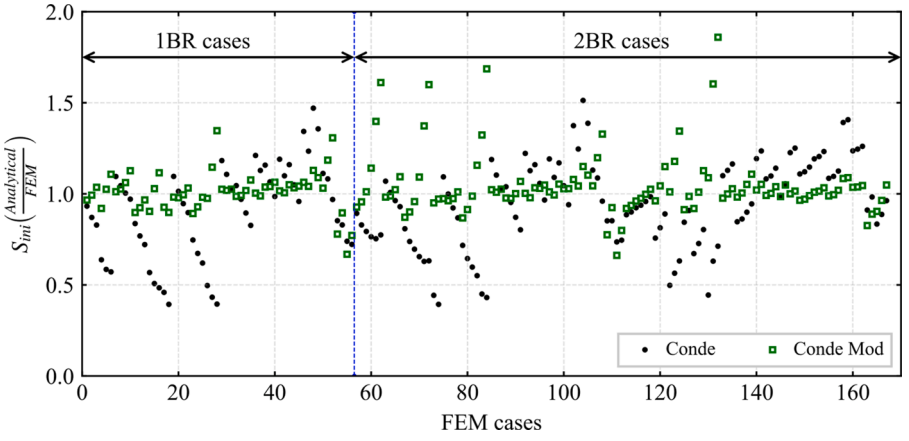

Fig. 40. Comparison between original Conde model and improved formulation.

Table 8
Initial stiffness estimates – Analytical method improvement.

Case Group	S_{ini} Conde/S_{ini} FEM					S_{ini} Conde Mod/S_{ini} FEM				
	Min [-]	Max [-]	Avg [-]	CoV [%]	RMSE [%]	Min [-]	Max [-]	Avg [-]	CoV [%]	RMSE [%]
1BR M14	0.57	1.10	0.85	21.5	23.4	0.92	1.13	1.03	5.7	6.5
1BR M20	0.39	0.84	0.59	25.6	43.5	0.90	1.12	0.96	7.6	8.4
1BR M25	0.39	1.10	0.73	32.4	35.8	0.89	1.35	1.03	12.1	12.7
1BR M30	0.83	1.18	1.01	11.2	11.3	0.99	1.08	1.02	2.7	3.4
1BR M35	0.99	1.21	1.11	7.0	13.5	0.99	1.07	1.03	2.6	3.8
1BR M40	0.96	1.19	1.09	7.5	12.2	1.01	1.05	1.03	1.6	3.3
1BR M45	1.23	1.47	1.35	6.3	36.3	1.04	1.13	1.08	3.1	8.9
1BR M60	0.97	1.11	1.05	5.4	7.7	1.03	1.31	1.17	10.0	20.9
1BR M70	0.83	0.85	0.84	1.1	16.3	0.77	0.89	0.83	7.2	17.7
1BR M80	0.73	0.74	0.73	0.5	26.8	0.67	0.78	0.72	7.8	28.4
1BR Total	**0.39**	**1.47**	**0.90**	**28.9**	**27.8**	**0.67**	**1.35**	**1.01**	**10.8**	**10.9**
2BR P1 M14	0.75	1.07	0.88	12.1	16.2	0.93	1.61	1.11	18.9	23.8
2BR P1 M20	0.39	0.81	0.62	21.1	39.8	0.87	1.60	1.09	22.3	25.9
2BR P1 M25	0.43	1.09	0.73	30.3	35.1	0.87	1.69	1.09	21.7	25.1
2BR P1 M30	0.80	1.19	1.00	12.3	12.3	0.98	1.07	1.01	3.0	3.2
2BR P1 M35	0.97	1.22	1.11	8.0	13.8	0.98	1.05	1.02	2.4	3.1
2BR P1 M40	0.94	1.19	1.09	8.4	12.6	0.99	1.05	1.02	1.8	3.0
2BR P1 M45	1.25	1.52	1.38	6.9	39.3	1.04	1.15	1.09	3.6	10.3
2BR P1 M60	0.96	1.13	1.05	6.9	9.1	1.04	1.32	1.18	9.7	21.8
2BR P1 M70	0.85	0.86	0.85	0.1	14.5	0.78	0.93	0.85	8.6	16.5
2BR P1 M80	0.74	0.74	0.74	0.1	25.7	0.67	0.80	0.73	8.9	27.6
2BR P2 M14	0.50	0.98	0.82	18.6	23.7	0.92	1.34	1.03	11.4	12.2
2BR P2 M20	0.44	0.91	0.73	17.8	30.2	0.87	1.86	1.15	28.1	35.9
2BR P2 M25	0.85	1.16	1.00	12.0	12.1	0.97	1.11	1.02	4.3	4.6
2BR P2 M30	0.99	1.24	1.11	7.0	13.7	0.99	1.05	1.02	2.2	3.1
2BR P2 M35	1.11	1.25	1.18	4.7	18.8	0.96	1.02	0.99	1.8	2.0
2BR P2 M40	1.08	1.23	1.16	4.9	16.5	0.99	1.03	1.01	1.5	1.8
2BR P2 M45	1.24	1.41	1.32	5.5	32.8	1.04	1.09	1.06	2.1	6.6
2BR P2 M70	0.84	0.98	0.91	5.6	10.7	0.78	1.05	0.90	9.9	13.3
2BR Total	**0.39**	**1.52**	**0.95**	**24.6**	**23.9**	**0.67**	**1.86**	**1.04**	**16.3**	**17.5**
Total	**0.39**	**1.52**	**0.94**	**26.1**	**25.2**	**0.67**	**1.86**	**1.03**	**14.9**	**15.7**

• P1 and P2 denote Pairs 1 and 2, respectively.

higher than 0.85, resulting in overestimation, and high μ welded columns, resulting in underestimation. In the remaining 89.2 % of the analyzed cases, the calibrated model exhibits a noteworthy proficiency in accurately predicting the initial stiffness of the face plate component. The root mean square error (RMSE) between observed and predicted values has been further reduced, decreasing from 27.8 % to 10.9 % in one-bolt row cases and from 23.9 % to 17.5 % in two-bolt row cases with the proposed improvement.

7. Conclusions

This paper reports on a study of the behavior of column webs/faces under out-of-plane loading in steel joints that provides experimental, numerical and design guidance for this joint component, as it is not currently characterized in design standards, namely in EN 1993–1–8 [25].

The following conclusions and contributions could be reached:

- A design proposal based on simple analytical expressions for the prediction of the initial stiffness of the face plate component was proposed, using the equivalent grillage model developed by Conde et al. [23]. Specifically, the width of the equivalent face plate was defined, providing excellent agreement when compared to the experimental test results and the large numerical parametric study.
- It was shown that the Neves model for initial stiffness provided poor results, while the Park and Wang formulation leads to reasonable results for 1 bolt row configurations but poor results for 2 bolt row configurations because it neglects group effects.
- The experimental results have highlighted that significant membrane effects are present in many cases, significantly increasing the design resistance of this component.
- The experimental results and the parametric study have identified the key parameters that affect the behavior of the face plate component: plate slenderness (μ), ratio of loaded area versus face plate width (α and β) and the flange support stiffness.

Finally, in this paper, the behavior of the face plate component was characterized without considering interactions from additional effects such as axial load [37] and transverse force acting simultaneously on the column web. The influence of these interactions will be reported in a future companion paper, also based on experimental tests and advanced numerical simulation.

CRediT authorship contribution statement

Melaku Seyoum Lemma: Writing – review & editing, Writing – original draft, Visualization, Validation, Software, Investigation, Formal analysis, Data curation. **Carlos Rebelo:** Writing – review & editing, Supervision, Methodology, Conceptualization. **Jorge Conde Conde:** Writing – review & editing, Supervision. **Luís Simões da Silva:** Writing – review & editing, Writing – original draft, Validation, Supervision, Methodology, Investigation, Conceptualization.

Declaration of competing interest

The authors declare that they have no known competing financial interests or personal relationships that could have appeared to influence the work reported in this paper.

Data availability

Data will be made available on request.

Acknowledgments

This work was partly financed by:

- FCT / MCTES through national funds (PIDDAC) under the R&D Unit Institute for Sustainability and Innovation in Structural Engineering (ISISE), under reference UIDB / 04029/2020, and under the Associate Laboratory Advanced Production and Intelligent Systems (ARISE) under reference LA/P/0112/2020.
- The doctoral grant 2020.07414.BD (https://doi.org/10.54499/2020.07414.BD) by the Portuguese Foundation for Science and Technology (FCT) attributed to the first author.
- Grant with reference UP2021–035 (RD 289/2021) from "Ministerio de Universidades de España", funded by European Union, NextGenerationEU, attributed to the third author.

Appendix A

Table A1
Parametric study one bolt row cases.

Case	Profile	Bolt spacing	Geom. Ratios	Sini. (FEM)	Sini. (Analytical)				Sini. (Analytical/FEM)			
					Park	Neves	Conde	Conde [Mod]	Park	Neves	Conde	Conde [Mod]
		[mm.]	[-]	[MN/m]	[MN/m]	[MN/m]	[MN/m]	[MN/m]	[-]	[-]	[-]	[-]
1	HE320C	P65, W0	μ14, β48%, α20%	131.4	212.5	78.4	122.5	126.9	1.62	0.60	0.93	0.97
2	HE320C	P90, W0	μ14, β60%, α20%	158.6	253.2	65.1	138.0	157.5	1.60	0.41	0.87	0.99
3	HE320C	P110, W0	μ14, β68%, α20%	188.0	299.3	63.6	155.8	194.7	1.59	0.34	0.83	1.04
4	HE320C	P135, W0	μ14, β80%, α20%	294.2	386.6	72.8	187.7	270.6	1.31	0.25	0.64	0.92
5	HE320C	P160, W0	μ14, β91%, α20%	404.1	541.5	103.8	236.4	414.2	1.34	0.26	0.59	1.03
6	HE320C	P170, W0	μ14, β95%, α20%	460.5	643.0	137.3	263.2	510.0	1.40	0.30	0.57	1.11
7	HE400M	P90, W0	μ14, β45%, α15%	163.5	279.2	99.3	179.1	165.4	1.71	0.61	1.10	1.01
8	HE400M	P120, W0	μ14, β55%, α15%	193.7	327.9	79.8	202.4	198.8	1.69	0.41	1.04	1.03
9	HE400M	P150, W0	μ14, β65%, α15%	235.3	397.6	74.4	236.3	249.8	1.69	0.32	1.00	1.06
10	HE400M	P180, W0	μ14, β75%, α15%	294.7	503.7	80.5	286.1	332.1	1.71	0.27	0.97	1.13
11	HE320B	P65, W0	μ20, β45%, α16%	55.3	78.9	73.3	46.3	49.6	1.43	1.33	0.84	0.90
12	HE320B	P90, W0	μ20, β56%, α16%	68.1	94.0	58.9	52.3	62.9	1.38	0.86	0.77	0.92
13	HE320B	P110, W0	μ20, β65%, α16%	82.3	111.1	56.6	59.4	79.5	1.35	0.69	0.72	0.97
14	HE320B	P135, W0	μ20, β76%, α16%	127.0	143.5	64.1	72.1	114.8	1.13	0.50	0.57	0.90
15	HE320B	P160, W0	μ20, β88%, α16%	181.3	201.1	90.3	92.0	186.4	1.11	0.50	0.51	1.03
16	HE320B	P170, W0	μ20, β92%, α16%	213.0	238.7	115.4	103.1	237.6	1.12	0.54	0.48	1.12
17	HE200A	P65, W0	μ21, β76%, α28%	59.8	56.1	46.4	27.4	55.4	0.94	0.78	0.46	0.93
18	HE200A	P80, W0	μ21, β87%, α28%	83.8	72.5	65.8	33.0	75.2	0.87	0.79	0.39	0.90
19	HE450B	P70, W0	μ25, β31%, α11%	38.0	54.4	93.2	41.6	37.3	1.43	2.45	1.10	0.98
20	HE450B	P105, W0	μ25, β41%, α11%	45.6	62.4	121.3	46.2	44.6	1.37	2.66	1.01	0.98
21	HE450B	P140, W0	μ25, β51%, α11%	56.3	73.5	76.0	53.3	56.0	1.31	1.35	0.95	1.00
22	HE450B	P170, W0	μ25, β60%, α11%	69.2	86.7	70.2	62.1	71.4	1.25	1.01	0.90	1.03
23	HE320A	P65, W0	μ25, β45%, α16%	30.2	37.8	80.9	22.5	26.9	1.25	2.68	0.75	0.89
24	HE320A	P90, W0	μ25, β56%, α16%	38.0	45.1	54.3	25.6	35.3	1.19	1.43	0.67	0.93
25	HE320A	P110, W0	μ25, β65%, α16%	46.9	53.3	52.9	29.1	46.0	1.14	1.13	0.62	0.98
26	HE320A	P135, W0	μ25, β76%, α16%	71.5	68.8	61.3	35.5	69.7	0.96	0.86	0.50	0.98
27	HE320A	P160, W0	μ25, β88%, α16%	105.5	96.4	90.4	45.6	120.9	0.91	0.86	0.43	1.15
28	HE320A	P175, W0	μ25, β94%, α16%	138.6	126.1	141.3	54.7	186.6	0.91	1.02	0.39	1.35
29	HE550B	P90, W0	μ29, β29%, α8%	30.0	41.3	69.0	35.5	30.8	1.38	2.30	1.18	1.03
30	HE550B	P130, W0	μ29, β38%, α8%	35.5	46.7	86.9	39.3	36.2	1.32	2.44	1.11	1.02
31	HE550B	P175, W0	μ29, β48%, α8%	44.5	55.0	88.8	45.9	45.6	1.24	2.00	1.03	1.03
32	HE450A	P70, W0	μ30, β31%, α11%	22.5	30.1	52.3	23.5	22.2	1.34	2.32	1.04	0.99
33	HE450A	P100, W0	μ30, β40%, α11%	26.5	33.8	65.6	25.7	26.3	1.28	2.48	0.97	0.99
34	HE450A	P135, W0	μ30, β50%, α11%	33.0	39.7	89.4	29.5	33.6	1.20	2.71	0.89	1.02
35	HE450A	P170, W0	μ30, β60%, α11%	42.7	48.1	65.6	35.3	45.9	1.13	1.54	0.83	1.08
36	HE700B	P115, W0	μ34, β26%, α6%	26.1	33.8	54.2	31.6	26.2	1.30	2.08	1.21	1.01
37	HE700B	P175, W0	μ34, β36%, α6%	31.7	38.8	69.9	35.8	31.3	1.22	2.20	1.13	0.99
38	HE550A	P85, W0	μ35, β28%, α8%	17.9	23.6	39.2	20.7	18.6	1.32	2.19	1.16	1.04
39	HE550A	P130, W0	μ35, β38%, α8%	21.8	27.1	50.8	23.2	22.7	1.24	2.33	1.06	1.04
40	HE550A	P175, W0	μ35, β48%, α8%	27.6	31.8	69.2	27.2	29.4	1.16	2.51	0.99	1.07
41	HE700A	P115, W0	μ40, β26%, α6%	16.7	21.0	33.8	19.9	17.0	1.25	2.02	1.19	1.01
42	HE700A	P175, W0	μ40, β36%, α6%	20.5	24.1	43.7	22.5	20.6	1.17	2.13	1.10	1.01
43	HE600AA	P95, W0	μ41, β27%, α8%	10.9	17.0	28.0	12.6	11.4	1.55	2.56	1.16	1.05
44	HE600AA	P145, W0	μ41, β37%, α8%	13.4	19.5	36.3	14.1	13.8	1.46	2.71	1.05	1.04
45	HE600AA	P195, W0	μ41, β48%, α8%	17.0	22.9	49.4	16.3	17.7	1.35	2.90	0.96	1.04
46	HE800A	P65, W0	μ45, β15%, α5%	11.6	15.5	22.0	15.6	12.3	1.34	1.91	1.35	1.07
47	HE800A	P135, W0	μ45, β26%, α5%	13.7	17.4	27.4	16.9	14.3	1.27	2.00	1.23	1.04
48	HE1000B	P85, W0	μ46, β14%, α4%	13.7	19.0	26.6	20.1	15.5	1.39	1.95	1.47	1.13
49	HE1000B	P175, W0	μ46, β24%, α4%	16.2	21.3	33.0	22.0	17.6	1.32	2.04	1.36	1.09
50	HG520 × 300	P60, W0	μ60, β21%, α8%	5.0	4.8	8.3	5.6	5.2	0.95	1.65	1.11	1.03
51	HG520 × 300	P120, W0	μ60, β33%, α8%	5.9	5.5	11.3	6.4	7.0	0.93	1.90	1.07	1.18
52	HG520 × 300	P180, W0	μ60, β46%, α8%	8.2	6.7	16.6	7.9	10.7	0.82	2.03	0.97	1.31
53	HG600 × 300	P70, W0	μ70, β19%, α7%	4.9	3.5	5.9	4.2	3.8	0.71	1.19	0.85	0.77
54	HG600 × 300	P140, W0	μ70, β32%, α7%	5.8	4.1	7.9	4.8	5.2	0.70	1.37	0.83	0.89
55	HG680 × 300	P80, W0	μ80, β19%, α6%	4.4	2.7	4.4	3.3	2.9	0.61	0.99	0.74	0.67
56	HG680 × 300	P160, W0	μ80, β31%, α6%	5.2	3.1	5.9	3.8	4.0	0.60	1.14	0.73	0.78

Table A2
Parametric study 2 bolt rows cases (Pairs 1).

Case	Profile	Bolt spacing	Geom. Ratios	Sini. (FEM)	Sini. (Analytical)				Sini. (Analytical/FEM)			
					Park	Neves	Conde	Conde [Mod]	Park	Neves	Conde	Conde [Mod]
		[mm.]	[-]	[MN/m]	[MN/m]	[MN/m]	[MN/m]	[MN/m]	[-]	[-]	[-]	[-]
57	HE320C	P65, W65	μ14, β48%, α48%	167.9	425.0	118.4	149.9	155.7	2.53	0.70	0.89	0.93
58	HE320C	P90, W75	μ14, β60%, α53%	210.8	506.3	109.6	174.8	201.5	2.40	0.52	0.83	0.96
59	HE320C	P110, W85	μ14, β68%, α57%	257.6	598.6	119.6	204.4	260.6	2.32	0.46	0.79	1.01
60	HE320C	P135, W95	μ14, β80%, α62%	335.5	773.2	158.3	256.3	382.8	2.30	0.47	0.76	1.14
61	HE320C	P160, W105	μ14, β91%, α66%	448.5	1083.0	273.4	338.0	626.9	2.41	0.61	0.75	1.40
62	HE320C	P170, W115	μ14, β95%, α71%	504.2	1286.0	407.1	390.5	812.3	2.55	0.81	0.77	1.61
63	HE400M	P90, W75	μ14, β45%, α40%	203.4	558.3	146.8	217.5	199.8	2.75	0.72	1.07	0.98
64	HE400M	P120, W85	μ14, β55%, α43%	251.3	655.8	129.9	253.3	248.4	2.61	0.52	1.01	0.99
65	HE400M	P150, W95	μ14, β65%, α47%	317.4	795.2	135.8	305.6	324.7	2.51	0.43	0.96	1.02
66	HE400M	P180, W105	μ14, β75%, α50%	413.0	1007.0	168.4	383.8	451.8	2.44	0.41	0.93	1.09
67	HE320B	P65, W60	μ20, β45%, α43%	69.6	157.8	108.1	56.3	60.7	2.27	1.55	0.81	0.87
68	HE320B	P90, W70	μ20, β56%, α48%	89.4	188.0	97.1	66.0	80.5	2.10	1.09	0.74	0.90
69	HE320B	P110, W80	μ20, β65%, α52%	111.6	222.2	104.7	77.7	106.8	1.99	0.94	0.70	0.96
70	HE320B	P135, W90	μ20, β76%, α56%	150.3	287.1	137.6	98.5	164.1	1.91	0.92	0.66	1.09
71	HE320B	P160, W100	μ20, β88%, α61%	209.7	402.1	236.2	131.9	287.9	1.92	1.13	0.63	1.37
72	HE320B	P170, W110	μ20, β92%, α65%	243.3	477.4	342.9	153.8	389.1	1.96	1.41	0.63	1.60
73	HE200A	P65, W60	μ21, β76%, α72%	82.9	112.2	91.0	36.7	78.8	1.35	1.10	0.44	0.95
74	HE200A	P80, W70	μ21, β87%, α80%	118.3	144.9	153.3	46.5	114.9	1.23	1.30	0.39	0.97
75	HE450B	P70, W60	μ25, β31%, α28%	44.2	108.7	120.9	48.3	43.0	2.46	2.73	1.09	0.97
76	HE450B	P105, W70	μ25, β41%, α31%	55.2	124.7	169.9	55.2	53.1	2.26	3.08	1.00	0.96
77	HE450B	P140, W80	μ25, β51%, α34%	71.0	146.9	116.7	65.5	69.1	2.07	1.64	0.92	0.97
78	HE450B	P170, W90	μ25, β60%, α37%	90.8	173.5	119.5	78.8	91.8	1.91	1.32	0.87	1.01
79	HE320A	P65, W60	μ25, β45%, α43%	38.3	75.6	119.5	27.5	33.2	1.98	3.12	0.72	0.87
80	HE320A	P90, W70	μ25, β56%, α48%	50.1	90.1	89.5	32.3	45.8	1.80	1.78	0.64	0.91
81	HE320A	P110, W80	μ25, β65%, α52%	63.8	106.5	97.7	38.1	63.0	1.67	1.53	0.60	0.99
82	HE320A	P135, W90	μ25, β76%, α56%	88.3	137.6	131.7	48.6	102.2	1.56	1.49	0.55	1.16
83	HE320A	P160, W100	μ25, β88%, α61%	145.9	192.7	236.4	65.7	193.0	1.32	1.62	0.45	1.32
84	HE320A	P175, W110	μ25, β94%, α65%	191.4	252.3	434.9	82.4	322.7	1.32	2.27	0.43	1.69
85	HE550B	P90, W60	μ29, β29%, α22%	33.9	82.7	85.5	40.3	34.7	2.44	2.52	1.19	1.02
86	HE550B	P130, W90	μ29, β38%, α29%	43.1	93.5	122.7	47.5	43.5	2.17	2.85	1.10	1.01
87	HE550B	P175, W120	μ29, β48%, α36%	57.5	110.0	146.5	59.3	59.0	1.91	2.55	1.03	1.03
88	HE450A	P70, W60	μ30, β31%, α28%	26.3	60.3	67.9	27.3	25.7	2.29	2.58	1.04	0.98
89	HE450A	P100, W70	μ30, β40%, α31%	32.2	67.7	91.4	30.7	31.4	2.11	2.84	0.95	0.98
90	HE450A	P135, W80	μ30, β50%, α34%	41.7	79.4	136.3	36.3	41.7	1.91	3.27	0.87	1.00
91	HE450A	P170, W90	μ30, β60%, α37%	56.0	96.1	111.6	44.9	59.8	1.72	1.99	0.80	1.07
92	HE700B	P115, W80	μ34, β26%, α20%	29.6	67.5	67.4	36.2	29.7	2.28	2.28	1.22	1.00
93	HE700B	P175, W100	μ34, β36%, α24%	37.7	77.5	94.9	42.5	36.9	2.05	2.51	1.13	0.98
94	HE550A	P85, W60	μ35, β28%, α22%	20.3	47.2	48.5	23.5	21.0	2.33	2.39	1.16	1.03
95	HE550A	P130, W70	μ35, β38%, α24%	25.6	54.1	67.1	27.1	26.4	2.11	2.62	1.06	1.03
96	HE550A	P175, W80	μ35, β48%, α27%	33.7	63.7	99.3	32.6	35.3	1.89	2.94	0.97	1.05
97	HE700A	P115, W60	μ40, β26%, α17%	18.5	41.9	40.0	22.0	18.7	2.27	2.17	1.19	1.01
98	HE700A	P175, W70	μ40, β36%, α18%	23.4	48.1	54.6	25.5	23.3	2.06	2.34	1.09	0.99
99	HE600AA	P95, W60	μ41, β27%, α20%	12.1	34.0	34.0	14.2	12.7	2.80	2.80	1.17	1.05
100	HE600AA	P145, W70	μ41, β37%, α22%	15.4	38.9	46.9	16.1	15.8	2.54	3.05	1.05	1.03
101	HE600AA	P195, W80	μ41, β48%, α24%	20.3	45.9	69.0	19.1	20.9	2.26	3.39	0.94	1.03
102	HE800A	P65, W60	μ45, β15%, α14%	12.4	30.9	25.1	17.0	13.4	2.50	2.02	1.38	1.08
103	HE800A	P135, W70	μ45, β26%, α16%	15.1	34.7	32.5	18.8	15.7	2.30	2.15	1.25	1.04
104	HE1000B	P85, W70	μ46, β14%, α12%	14.5	37.9	30.0	21.9	16.7	2.62	2.08	1.52	1.15
105	HE1000B	P175, W90	μ46, β24%, α15%	17.7	42.6	39.3	24.6	19.5	2.41	2.22	1.39	1.10
106	HG520 × 300	P60, W60	μ59, β21%, α21%	5.6	9.5	10.0	6.3	5.8	1.70	1.78	1.13	1.04
107	HG520 × 300	P120, W80	μ59, β33%, α25%	7.0	11.1	15.0	7.6	8.4	1.58	2.14	1.08	1.19
108	HG520 × 300	P180, W100	μ59, β46%, α29%	10.4	13.4	25.2	10.0	13.8	1.28	2.41	0.96	1.32
109	HG600 × 300	P70, W60	μ69, β19%, α18%	5.5	7.0	6.9	4.7	4.3	1.28	1.26	0.86	0.78
110	HG600 × 300	P140, W80	μ69, β32%, α21%	6.6	8.1	10.2	5.6	6.1	1.24	1.55	0.85	0.93
111	HG680 × 300	P80, W60	μ79, β19%, α15%	4.9	5.4	5.1	3.6	3.2	1.10	1.04	0.74	0.67
112	HG680 × 300	P160, W80	μ79, β31%, α19%	5.8	6.2	7.4	4.3	4.6	1.07	1.27	0.74	0.80

Table A3
Parametric study 2 bolt rows cases (Pairs 2).

Case	Profile	Bolt spacing	Geom. Ratios	Sini. (FEM)	Sini. (Analytical)				Sini. (Analytical/FEM)			
					Park	Neves	Conde	Conde [Mod]	Park	Neves	Conde	Conde [Mod]
		[mm.]	[-]	[MN/m]	[MN/m]	[MN/m]	[MN/m]	[MN/m]	[-]	[-]	[-]	[-]
113	HE320C	P65, W65	μ14, β48%, α48%	167.9	425.0	118.4	149.9	155.7	2.53	0.70	0.89	0.93
114	HE320C	P65, W85	μ14, β48%, α57%	178.9	425.0	130.7	158.3	164.5	2.37	0.73	0.88	0.92
115	HE320C	P65, W105	μ14, β48%, α66%	185.2	425.0	143.0	166.8	173.4	2.29	0.77	0.90	0.94
116	HE320C	P65, W125	μ14, β48%, α75%	189.7	425.0	155.2	175.2	182.2	2.24	0.82	0.92	0.96

(*continued on next page*)

Table A3 (*continued*)

Case	Profile	Bolt spacing	Geom. Ratios	Sini. (FEM)	Sini. (Analytical)				Sini. (Analytical/FEM)			
					Park	Neves	Conde	Conde [Mod]	Park	Neves	Conde	Conde [Mod]
		[mm.]	[-]	[MN/m]	[MN/m]	[MN/m]	[MN/m]	[MN/m]	[-]	[-]	[-]	[-]
117	HE320C	P65, W145	μ14, β48%, α84%	195.9	425.0	167.5	183.6	191.1	2.17	0.86	0.94	0.98
118	HE320C	P65, W165	μ14, β48%, α93%	200.5	425.0	179.8	192.0	199.9	2.12	0.90	0.96	1.00
119	HE320C	P65, W185	μ14, β48%, α10%	203.7	425.0	192.1	200.5	208.8	2.09	0.94	0.98	1.02
120	HE320C	P110, W65	μ14, β68%, α48%	254.9	598.6	106.5	192.9	245.1	2.35	0.42	0.76	0.96
121	HE320C	P110, W125	μ14, β68%, α75%	279.3	598.6	146.0	227.2	291.5	2.14	0.52	0.81	1.04
122	HE320C	P110, W185	μ14, β68%, α10%	294.0	598.6	185.6	261.5	338.0	2.04	0.63	0.89	1.15
123	HE320C	P170, W65	μ14, β95%, α48%	673.6	1286.0	289.8	335.1	680.8	1.91	0.43	0.50	1.01
124	HE320C	P170, W125	μ14, β95%, α75%	711.7	1286.0	430.6	401.5	838.6	1.81	0.61	0.56	1.18
125	HE320C	P170, W185	μ14, β95%, α10%	741.1	1286.0	571.4	467.9	996.3	1.74	0.77	0.63	1.34
126	HE320B	P65, W60	μ20, β45%, α43%	69.6	157.8	108.1	56.3	60.7	2.27	1.55	0.81	0.87
127	HE320B	P65, W120	μ20, β45%, α70%	78.5	157.8	143.0	66.2	71.7	2.01	1.82	0.84	0.91
128	HE320B	P65, W180	μ20, β45%, α96%	83.9	157.8	177.9	76.2	82.7	1.88	2.12	0.91	0.99
129	HE320B	P110, W60	μ20, β65%, α43%	108.8	222.2	92.7	73.1	100.0	2.04	0.85	0.67	0.92
130	HE320B	P110, W120	μ20, β65%, α70%	119.4	222.2	128.7	86.8	120.5	1.86	1.08	0.73	1.01
131	HE320B	P110, W180	μ20, β65%, α96%	125.1	222.2	164.7	100.5	141.0	1.78	1.32	0.80	1.13
132	HE320B	P170, W60	μ20, β92%, α43%	294.3	477.4	239.5	130.7	320.3	1.62	0.81	0.44	1.09
133	HE320B	P170, W120	μ20, β92%, α70%	251.3	477.4	363.5	158.4	402.9	1.90	1.45	0.63	1.60
134	HE320B	P170, W180	μ20, β92%, α96%	261.1	477.4	487.6	186.0	485.6	1.83	1.87	0.71	1.86
135	HE450B	P70, W60	μ25, β31%, α28%	44.2	108.7	120.9	48.3	43.0	2.46	2.73	1.09	0.97
136	HE450B	P70, W100	μ25, β31%, α40%	48.0	108.7	139.4	52.8	46.9	2.26	2.90	1.10	0.98
137	HE450B	P70, W140	μ25, β31%, α51%	50.7	108.7	157.8	57.2	50.7	2.14	3.11	1.13	1.00
138	HE450B	P70, W180	μ25, β31%, α63%	53.0	108.7	176.3	61.7	54.5	2.05	3.33	1.16	1.03
139	HE450B	P170, W60	μ25, β60%, α28%	86.5	173.5	103.1	73.2	85.0	2.01	1.19	0.85	0.98
140	HE450B	P170, W100	μ25, β60%, α40%	93.6	173.5	125.0	80.7	94.0	1.85	1.34	0.86	1.01
141	HE450B	P170, W140	μ25, β60%, α51%	98.0	173.5	146.9	88.1	103.1	1.77	1.50	0.90	1.05
142	HE450B	P170, W180	μ25, β60%, α63%	101.2	173.5	168.8	95.6	112.1	1.71	1.67	0.94	1.11
143	HE550B	P90, W60	μ29, β29%, α22%	33.9	82.7	85.5	40.3	34.7	2.44	2.52	1.19	1.02
144	HE550B	P90, W120	μ29, β29%, α36%	37.8	82.7	102.1	45.1	38.6	2.19	2.70	1.19	1.02
145	HE550B	P90, W180	μ29, β29%, α50%	40.4	82.7	118.7	49.9	42.5	2.05	2.94	1.24	1.05
146	HE550B	P130, W60	μ29, β38%, α22%	41.4	93.5	110.8	44.8	41.0	2.26	2.67	1.08	0.99
147	HE550B	P130, W120	μ29, β38%, α36%	45.8	93.5	134.7	50.3	45.9	2.04	2.94	1.10	1.00
148	HE550B	P130, W180	μ29, β38%, α50%	48.9	93.5	158.6	55.8	50.8	1.91	3.24	1.14	1.04
149	HE550B	P175, W60	μ29, β48%, α22%	53.1	110.0	117.7	52.6	52.3	2.07	2.22	0.99	0.99
150	HE550B	P175, W120	μ29, β48%, α36%	57.5	110.0	146.5	59.3	59.0	1.91	2.55	1.03	1.03
151	HE550B	P175, W180	μ29, β48%, α50%	62.6	110.0	175.4	66.0	65.6	1.76	2.80	1.05	1.05
152	HE700B	P115, W80	μ34, β26%, α20%	29.6	67.5	67.4	36.2	29.7	2.28	2.28	1.22	1.00
153	HE700B	P115, W140	μ34, β26%, α30%	32.3	67.5	77.3	39.6	32.3	2.09	2.39	1.23	1.00
154	HE700B	P115, W200	μ34, β26%, α41%	34.4	67.5	87.3	43.0	34.9	1.97	2.54	1.25	1.02
155	HE700B	P175, W80	μ34, β36%, α20%	37.1	77.5	89.9	41.1	35.8	2.09	2.42	1.11	0.96
156	HE700B	P175, W140	μ34, β36%, α30%	40.3	77.5	104.9	45.2	39.1	1.92	2.60	1.12	0.97
157	HE700B	P175, W200	μ34, β36%, α41%	42.9	77.5	119.8	49.2	42.5	1.81	2.80	1.15	0.99
158	HE700A	P115, W80	μ40, β26%, α20%	19.1	41.9	42.1	22.8	19.3	2.19	2.20	1.19	1.01
159	HE700A	P115, W140	μ40, β26%, α30%	20.7	41.9	48.3	24.9	21.0	2.02	2.33	1.21	1.01
160	HE700A	P115, W200	μ40, β26%, α41%	22.0	41.9	54.4	27.1	22.7	1.90	2.47	1.23	1.03
161	HE700A	P175, W80	μ40, β36%, α20%	23.9	48.1	56.2	25.9	23.6	2.01	2.35	1.08	0.99
162	HE700A	P175, W140	μ40, β36%, α30%	26.0	48.1	65.5	28.5	25.9	1.85	2.52	1.10	1.00
163	HE700A	P175, W200	μ40, β36%, α41%	27.6	48.1	74.9	31.1	28.1	1.74	2.71	1.12	1.02
164	HE800A	P65, W60	μ45, β15%, α14%	12.4	30.9	25.1	17.0	13.4	2.50	2.02	1.38	1.08
165	HE800A	P65, W120	μ45, β15%, α23%	13.3	30.9	28.1	18.5	14.4	2.32	2.11	1.39	1.08
166	HE800A	P65, W180	μ45, β15%, α32%	14.2	30.9	31.1	20.0	15.5	2.18	2.20	1.41	1.09
167	HE800A	P135, W60	μ45, β26%, α14%	15.0	34.7	31.8	18.5	15.5	2.32	2.12	1.24	1.04
168	HE800A	P135, W120	μ45, β26%, α23%	16.2	34.7	36.2	20.2	16.8	2.14	2.23	1.24	1.04
169	HE800A	P135, W180	μ45, β26%, α32%	17.3	34.7	40.5	21.8	18.1	2.01	2.35	1.26	1.05
170	HG600 × 300	P70, W60	μ69, β19%, α18%	5.5	7.0	6.9	4.7	4.3	1.28	1.26	0.86	0.78
171	HG600 × 300	P70, W120	μ69, β19%, α28%	5.7	7.0	8.0	5.2	4.7	1.22	1.39	0.91	0.82
172	HG600 × 300	P70, W180	μ69, β19%, α39%	5.8	7.0	9.0	5.7	5.2	1.20	1.54	0.98	0.88
173	HG600 × 300	P140, W60	μ69, β32%, α18%	6.5	8.1	9.7	5.4	5.9	1.26	1.50	0.84	0.91
174	HG600 × 300	P140, W120	μ69, β32%, α28%	6.8	8.1	11.4	6.0	6.6	1.21	1.69	0.89	0.97
175	HG600 × 300	P140, W180	μ69, β32%, α39%	6.9	8.1	13.1	6.6	7.2	1.18	1.90	0.96	1.05

References

[1] Janss, J., Jaspart, J.-P., Maquoi, R.: Strength and behaviour of in-plane weak axis joints and of 3-D joints. 60–68 (1988).

[2] J.A. Packer, G.A. Morris, G. Davies, A limit states design method for welded tension connections to I-section webs, J. Constr. Steel Res. 12 (1989) 33–53, https://doi.org/10.1016/0143-974X(89)90048-5.

[3] L.R.O. de Lima, S.A.L. de Andrade, S. da, P.C.G. Vellasco, L.S. da Silva, Experimental and mechanical model for predicting the behaviour of minor axis beam-to-column semi-rigid joints, Int. J. Mech. Sci. 44 (2002) 1047–1065, https://doi.org/10.1016/S0020-7403(02)00013-9.

[4] Chin, C.W., Sarkar, S., Virdi, K.S.: Behaviour of beam-to-column minor axis connections - a comprehensive investigation. (2003).

[5] Kim, S.D., Kim, S.S., Ju, Y.K.: Strength evaluation of beam-column connection in the weak axis of H-shaped column, (2008).

[6] M.A. Dabaon, M.H. El-Boghdadi, O.F. Kharoob, Experimental and numerical model for space steel and composite semi-rigid joints, J. Constr. Steel Res. 65 (2009) 1864–1875, https://doi.org/10.1016/j.jcsr.2009.04.024.

[7] J.D. Gao, H.X. Yuan, H. Qian, X.W. Chen, Structural behaviour and design of stainless steel end-plate beam-to-exterior column minor-axis joints, Thin-Walled Struct. 181 (2022) 110119, https://doi.org/10.1016/J.TWS.2022.110119.

[8] J. Pan, S. Chen, Z. Wang, H. Lu, Initial rotational stiffness of minor-axis flush end-plate connections, Adv. Mech. Eng. 10 (2018) 2018, https://doi.org/10.1177/1687814017745397.
[9] S. Chen, Z. Wang, C. Zhou, P. Chen, Experimental investigation on the mechanical behavior of semi-rigid composite joints loaded along the minor-axis, Open Civ. Eng. J. 9 (2015) 12–20, https://doi.org/10.2174/1874149501509010012.
[10] M. Md Tahir, I. Juki, L.H. Yong, S. Mohammad, S.P. Ngian, Finite element analysis of flush end-plate connections connected to column web, Int. J. Steel Struct. 11 (2011) 247–258, https://doi.org/10.1007/s13296-011-3001-3.
[11] A. Ghobarah, S. Mourad, R.M. Korol, Moment-rotation relationship of blind bolted connections for HSS columns, J. Constr. Steel Res. 40 (1996) 63–91, https://doi.org/10.1016/S0143-974X(96)00044-2.
[12] Z.Y. Wang, Q.Y. Wang, Yield and ultimate strengths determination of a blind bolted endplate connection to square hollow section column, Eng. Struct. 111 (2016) 345–369, https://doi.org/10.1016/j.engstruct.2015.11.058.
[13] I. García, M.A. Serrano, C. López-Colina, F.L. Gayarre, The strength of beam-to-RHS joints with welded studs, J. Build. Eng. 76 (2023) 107203, https://doi.org/10.1016/j.jobe.2023.107203.
[14] I. García, M.A. Serrano, C. López-Colina, F.L. Gayarre, The stiffness of beam-to-RHS joints with welded studs, J. Build. Eng. 70 (2023), https://doi.org/10.1016/j.jobe.2023.106340.
[15] M.A. Serrano-López, C. López-Colina, Y.C. Wang, M. Lozano, I. García, F. L. Gayarre, An experimental study of I beam-RHS column demountable joints with welded studs, J. Constr. Steel Res. 182 (2021), https://doi.org/10.1016/j.jcsr.2021.106651.
[16] L. Simões da Silva, M.S. Lemma, A.F. Santos, J. Conde, T. Tankova, Y. Harada, Design and behavior of beam-to-column joints connected to the column web or the faces of a tubular column, in: S.L. Chan, H.H. Lau (Eds.), Proceedings of the Eleventh International Conference on Advances in Steel Structures (ICASS), 2023. Malaysia.
[17] Neves, L.C., Gomes, F.: Semi-rigid behaviour of beam-to-column minor-axis joints. In: Proc., IABSE Int. Colloquium on Semi-Rigid Structural Connections. pp. 207–216., Istanbul (1996).
[18] Neves, L.C.: Monotonic and cyclic behavior of weak axis and tubular connections in steel and steel-concrete composite structures, Doctoral Thesis in Portuguese, (2004).
[19] L. Simões da Silva, L.F.N. Neves, F.C.T. Gomes, Rotational stiffness of rectangular hollow sections composite joints, J. Struct. Eng. 129 (2003) 487–494, https://doi.org/10.1061/(ASCE)0733-9445(2003)129:4(487).
[20] A.Y. Park, Y.C. Wang, Development of component stiffness equations for bolted connections to RHS columns, J. Constr. Steel Res. 70 (2012) 137–152, https://doi.org/10.1016/J.JCSR.2011.08.004.
[21] Park, A.Y.: Semi-rigid joints to tubular columns and their use in semi-continuous frame design, (2012).
[22] D. Ye, K. Ke, Y. Chen, Stiffness model for "column face in bending" component in tensile zone of bolted joints to SHS/RHS column, Steel Compos. Struct. 38 (2021) 637–656, https://doi.org/10.12989/scs.2021.38.6.637.
[23] J. Conde, L. Simões da Silva, A. Francisca Santos, M.S. Lemma, T. Tankova, A model for the initial stiffness of the face plate component, Eng. Struct. 295 (2023) 116836, https://doi.org/10.1016/j.engstruct.2023.116836.
[24] European Committee for Standardization (CEN): Eurocode 3: design of steel structures — part 1-8: design of joints, incorporating corrigenda Nos. 1 and 2. (2005).
[25] European Committee for Standardization (CEN): Eurocode 3: design of steel structures — part 1-8: joints (FprEN 1993-1-8:2023). (2023).
[26] Lemma, M.S., Simões Da Silva, L., Rebelo, C.: Column web/face characterization under out-of-plane and transverse loads, Experimental Campaign Report., Coimbra, Portugal (2023).
[27] Gomes, F.C.T.: Etat Limite Ultime De La Resistance De L'ame D'une Colone Dans Un Assemblage Semi-Rigid D'axe Faible Rapport Interne N° 203., Liège (1990).
[28] ISO: ISO 6892-1: Metallic materials: Tensile testing. Part 1. (2009).
[29] (CEN), E.C. for S.: EN 1090-2, execution of steel structures and aluminium structures part 2: technical requirements for steel structures. (2018).
[30] SIMULIA - Dassault Systèmes (3DS): Abaqus 2021, (2021).
[31] F. Yang, M. Veljkovic, Y. Liu, Ductile damage model calibration for high-strength structural steels, Constr. Build. Mater. 263 (2020) 120632, https://doi.org/10.1016/j.conbuildmat.2020.120632.
[32] L. Simões da Silva, H. Craveiro, J. Conde, R. Simões, C. Martins, A. Catinaccio, D. Mladenov, J.B. Lopes, D.A. Feito, C. Bault, Experimental behaviour of large-size beam-to-column steel joints for the DUNE Neutrino Experiment, Thin-Walled Struct. 191 (2023) 110996, https://doi.org/10.1016/j.tws.2023.110996.
[33] Y. Zhang, P. Kyvelou, Y. Wang, B. Li, Y. Ouyang, L. Gardner, Experimental investigation and design of slip resistant aluminium alloy–stainless steel connections, Thin-Walled Struct. 186 (2023) 110712, https://doi.org/10.1016/j.tws.2023.110712.
[34] European Committee for Standardization (CEN): prEN 1993-1-14: design of steel structures — part 1-14: design assisted by finite element analysis, (2023).
[35] X. Yun, L. Gardner, Stress-strain curves for hot-rolled steels, J. Constr. Steel Res. 133 (2017) 36–46, https://doi.org/10.1016/J.JCSR.2017.01.024.
[36] L. Costa Neves, L. Simões da Silva, P.C. Vellasco, A model for predicting the stiffness of beam to concrete filled column and minor axis joints under static monotonic loading, in: Proceedings of the Eurosteel 2005: 4th European Conference on Steel and Composite Structures C. C, 2005, pp. 410131–410138.
[37] J. Conde, F. Freire, F. Ljubinković, M. Vild, L.S. da Silva, Welded beam-to-column steel joints: assessment of European design rules, Thin-Walled Struct. (2024), https://doi.org/10.1016/J.TWS.2024.111844.